

Planar Microassembly by Parallel Actuation of MEMS Microrobots

Bruce R. Donald, *Member, IEEE*, Christopher G. Levey, *Member, IEEE*, and Igor Paprotny

Abstract—We present designs, theory, and results of fabrication and testing for a novel parallel microrobotic assembly scheme using stress-engineered MEMS microrobots. The robots are $240\text{--}280\ \mu\text{m} \times 60\ \mu\text{m} \times 7\text{--}20\ \mu\text{m}$ in size and can be controlled to dock compliantly together, forming planar structures several times this size. The devices are classified into *species* based on the design of their steering arm actuators, and the species are further classified as *independent* if they can be maneuvered independently using a single global control signal. In this paper, we show that microrobot species are independent if the two transition voltages of their steering arms, i.e., the voltages at which the arms are raised or lowered, form a unique pair. We present control algorithms that can be applied to groups of independent microrobot species to direct their motion from arbitrary nondead-lock configurations to desired planar microassemblies. We present designs and fabrication for four independent microrobot species, each with a unique transition voltage. The fabricated microrobots are used to demonstrate directed assembly of five types of planar structures from two classes of initial conditions. We demonstrate an average docking accuracy of $5\ \mu\text{m}$ and use self-aligning compliant interaction between the microrobots to further align and stabilize the intermediate assemblies. The final assemblies match their target shapes on average 96%, by area. [2007-0233]

Index Terms—Microactuators, microassembly, microelectromechanical systems (MEMS), microrobots, scratch-drive actuators.

I. INTRODUCTION

THIS PAPER presents designs, theory, and experimental results for a novel microassembly scheme, which aggregates planar structures from a group of parallel-actuated MEMS microrobots [1]. In this context, *parallel-actuated* (as opposed to serial) refers to the robots moving simultaneously under the application of a single global control and power-delivery signal. The robots are $240\text{--}280\ \mu\text{m} \times 60\ \mu\text{m} \times 7\text{--}20\ \mu\text{m}$ in size, and consist of untethered scratch-drive actuators (USDAs) [2] that provide forward motion and steering-arm actuators that control whether the robots move forward or turn.

Manuscript received September 26, 2007; revised April 1, 2008. First published July 2, 2008; last published August 1, 2008 (projected). This work was supported by grant number GM-65982 to B. R. Donald from NIH, and 2000-DT-CX-K001 to B. R. Donald, from the Office for Domestic Preparedness, Department of Homeland Security, USA. Subject Editor G. Fedder.

B. R. Donald is with the Department of Computer Science, Duke University, Durham, NC 27708-0129 USA, and also with the Department of Biochemistry, Duke University Medical Center, Durham, NC 27710 USA (e-mail: brd+jmems08@cs.duke.edu).

C. G. Levey is with the Thayer School of Engineering, Dartmouth College, Hanover, NH 03755 USA.

I. Paprotny is with the Department of Computer Science, Dartmouth College, Hanover, NH 03755 USA, and also with the Department of Computer Science, Duke University, Durham, NC 27708-0129 USA.

Color versions of one or more of the figures in this paper are available online at <http://ieeexplore.ieee.org>.

Digital Object Identifier 10.1109/JMEMS.2008.924251

We present fabrication methods, designs, control algorithms, and experimental results demonstrating the first simultaneous control of multiple untethered microrobots, and report the application of such multimicrorobotic systems to the assembly of planar microstructures. The aggregation and assembly of these structures is controlled and programmed by docking the individual robots, whereas defect formation is avoided by using noncolliding paths, enabling virtually defect-free assembly. The rigidity of the assembled structure is maintained through mutual compliant interaction between the immobilized robots and through electrostatic attraction to the substrate. We use the term *compliance* to denote the change of pose of one rigid body in accommodation to forces exerted by a second rigid body and friction [3].

Microrobots are often intentionally simple in design, in order to minimize their size, subject to feature-size constraints imposed by the microfabrication processes. Parallel operation and cooperation of many such devices has not been previously demonstrated. Consequently, our work required innovations in design, fabrication, and control algorithms to enable independent controllability through a broadcast control signal. We believe that our algorithms and the general design methodology can be applied to the control of other similarly underactuated micro- and, perhaps, nanorobotic systems.

The devices presented in this paper are fabricated using the commercially available PolyMUMPS process [4] followed by a custom stress-engineering processing step to add out-of-plane curvature to the steering-arm actuators. If necessary, a post-release trimming of the steering-arm actuators can be applied to further adjust the curvature of the steering arms. A batch transfer mechanism called a *transfer frame* is used to move groups of microrobots to their operating environment. While on the operating environment, the microrobots receive their electrical control and power-delivery signal through an array of underlying insulated electrodes, and all microrobots on the same operating environment receive the same, single, control and power-delivery signal. The robot chassis is composed of conductive (n-doped) polycrystalline silicon, such that the same voltage is induced on both the USDA and the connected steering arm.

Similar to an electrostatic cantilever beam [5], the steering arm of each microrobot has two distinct voltage levels at which the arm abruptly changes states. These are the *snap-down voltage* at which the arm is pulled in contact with the substrate as the robot is commanded to turn and the *release voltage* at which the arm is released when the robot is commanded to move straight. We call these voltage levels the *transition voltages* of the steering arm. The transition voltages are determined by the steering-arm designs. Microrobots with the

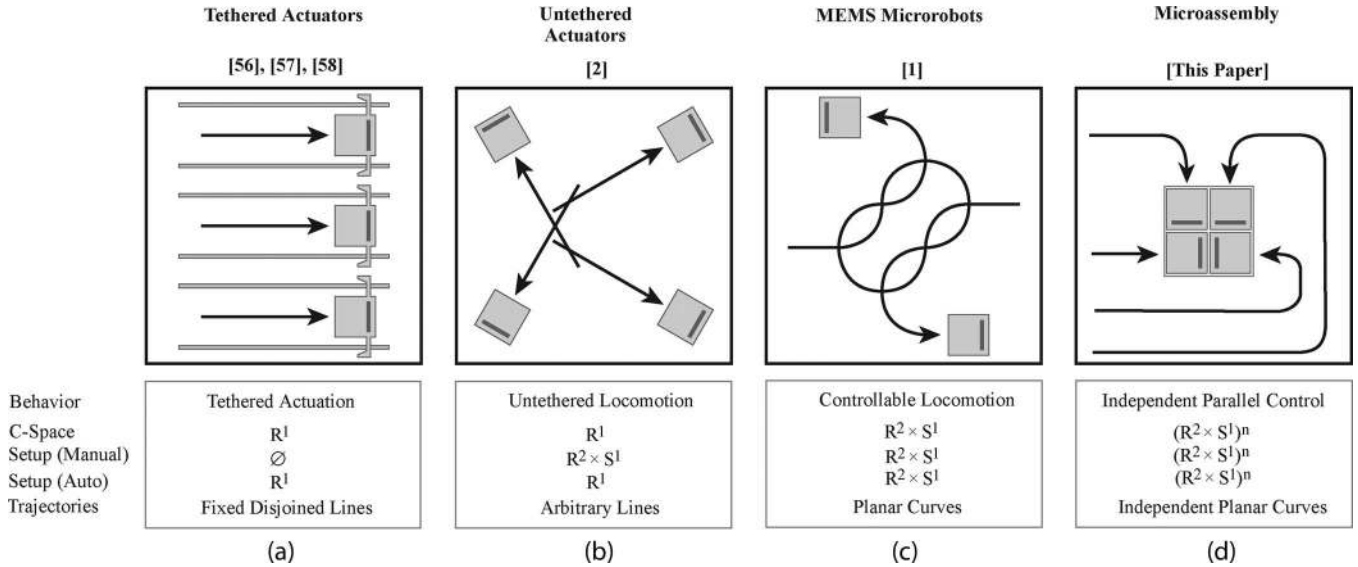


Fig. 1. Progress toward planar microassembly presented in this paper. *C-space* represents the total DOF of the device motion. *Setup* indicates the DOF possible through initialization of the device's pose (position and orientation) prior to motion either manually with a pair of microprobes (Manual) or in an automated fashion (Auto). Four classes of devices are shown. (a) Tethered scratch-drive actuators (SDAs) constrained to move along fixed lines or circles that map onto \mathbb{R}^1 in *C-space*. (b) Untethered actuators presented in [2]. These devices also operate in \mathbb{R}^1 but can be manually initialized in $\mathbb{R}^2 \times S^1$ moving along arbitrary lines in the plane. (c) Behavior of the microrobots presented in [1]. Although both nonholonomic and underactuated, these devices are capable of accessing all points in their *C-space* $\mathbb{R}^2 \times S^1$. (d) Capabilities of multimicrorobot control and assembly presented in this paper. We show how to implement microassembly by reducing the parallel control of n microrobots to parallel control of two devices, followed by sequential control of single robots. We use this control strategy to assemble planar microscale structures.

same steering-arm design are classified as the same *species*. The species are further classified as *independent* if they can be controlled as independent *nonholonomic*¹ systems during microassembly using a single global control and power-delivery signal. In this work, we achieve species independence by choosing steering-arm designs that provide a unique snap-down and release voltage *pair*; at least one of the transition voltages must be different between any two devices. Variability in the fabrication process and the power coupling to the microrobot necessitates a minimum separation between the voltage levels that are used for control, resulting in a finite number of accessible transition voltages, and an upper bound on the number of unique snap-down and release voltage pairs.

Fig. 1 shows the progression of our technology toward the implementation of microassembly and the devices presented in this paper. The stress-engineered MEMS microrobot, which is presented in [1], is nonholonomic because, from any point, the robot can only move forward in a straight-line motion or turn. It is also *underactuated*¹ because the degrees of freedom (DOF) of the control and power-delivery signal (voltage applied through the power-delivery substrate) are less than the DOF of its configuration. We show in [1] that, even though the system is nonholonomic and underactuated, turning and straight-line motion are sufficient for a single robot to reach all possible configurations, and the robot is *globally controllable*¹ [2].

A system of n microrobots operating within the same environment is still nonholonomic and highly underactuated, because all the robots receive a single common control signal. Since all n robots are electrically (and, via compliance, intermittently mechanically) coupled, the generalization of our

earlier work from 1 to n robots required advances in design, fabrication, control, and programming to defeat the coupling and the potentially exponential explosion in complexity due to added DOF of the configuration space (*C-space*). In this paper, we present microrobot designs that efficiently demultiplex the common control signal for a group of n microrobots, and a control strategy that implements microassembly, transforming the problem of parallel control of n devices to parallel control of two robots, followed by a sequential control of single robots. We used this control strategy to assemble several planar microstructures.

Fig. 2 shows scanning-electron micrographs of the five microrobot species, four of which are independent, that we used to implement microassembly. The micrographs of planar structures assembled by these microrobots are shown in Fig. 3. The final assemblies matched their target shapes (portion of the area of the target shape covered by the assembling structure) by 96%, on average. All assembly experiments were conducted within a small (2 mm^2) area.

The main contributions of this paper can be summarized as follows.

- 1) **Fabrication:** We extended the stress-engineering process from [1] to minimize process variability, successfully surmounting several challenges, including the inherent susceptibility of stress-engineered microrobots to galvanic attack (GA). We also developed a single-device trimming method that can be used to even further reduce any remaining processing error. Combined, these two technologies minimize the voltage separation required to sufficiently differentiate pairs of steering-arm transition voltages, enabling parallel control of multiple devices through a single control signal.

¹See Appendix. Definition of Terms.

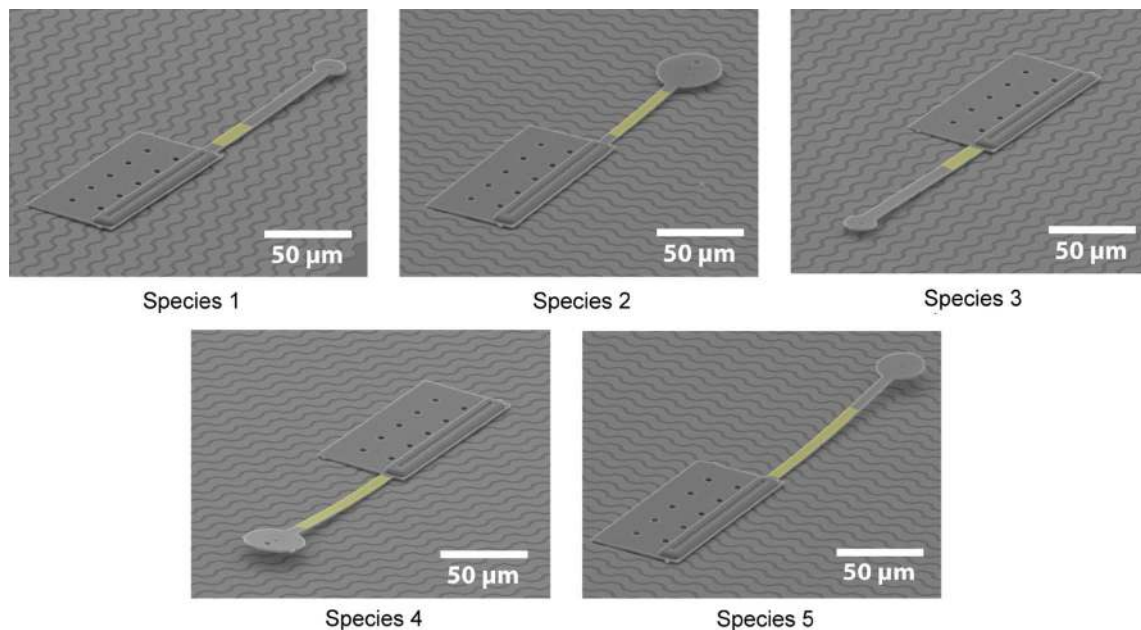


Fig. 2. Scanning-electron micrographs of the five microrobot species used to implement microassembly. Four of the species are independent. The systems of independent species are 1, 3, 4, 5 or 2, 3, 4, 5. The transition voltages of species 1 and 2 are similar, despite different steering-arm designs. Refer to Table III for the exact specification of the parameters for each of the steering-arm types. Yellow color is used to highlight the areas of the steering arms covered by the chrome layer.

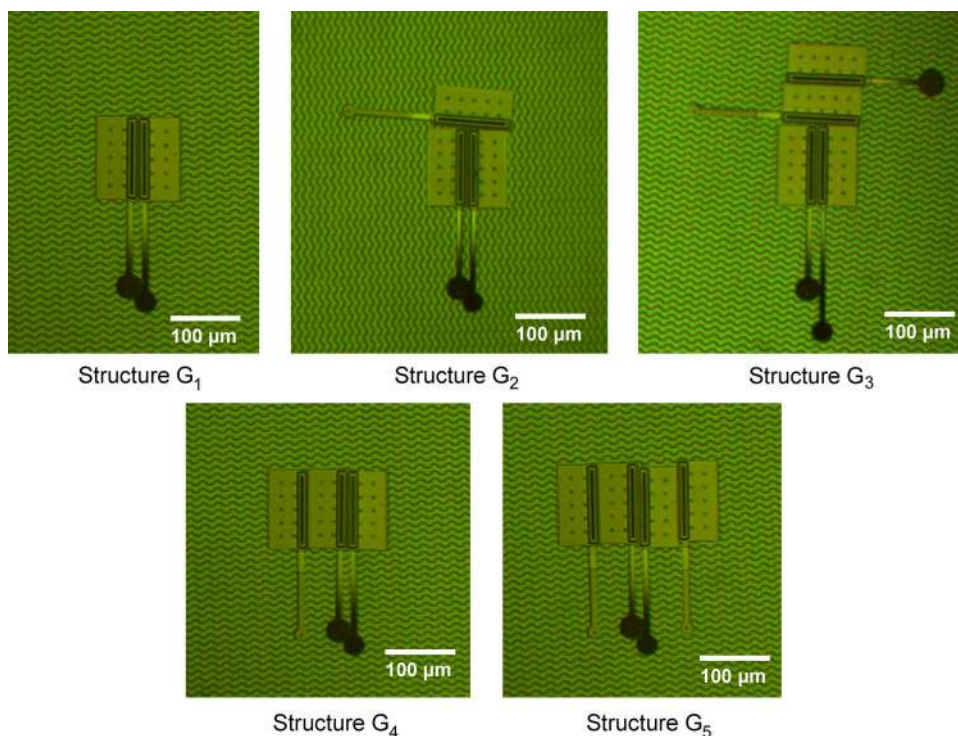


Fig. 3. Optical micrograph of planar structures assembled using microrobot species shown in Fig. 2. The example of structure G_3 was assembled using an earlier version of species 5 (lower right device), with a longer steering arm.

- 2) **Designs:** We present five novel steering-arm actuator designs with sufficiently separated transition voltages to permit parallel control of groups of up to four microrobots. The designs were developed through extensive modeling and experimentation, and represent a significant extension of the designs for single microrobot in isolation [1].
- 3) **Control:** We developed a control strategy for our microrobots that implements microassembly by exploiting design-induced differences between the transition voltages of their steering-arm actuators, transforming the problem of parallel control of multiple devices to parallel control of two robots, followed by successive sequential control of single robots. Our control scheme requires only

pairs of transition voltages to be unique, significantly reducing the necessary number of independent voltage levels required by the previously *proposed* approach [1].

- 4) **Experimental Testing:** We present the results of experiments and testing of the first implementation of an untethered multi-microrobotic system. We fabricated and tested 15 microrobots, and used these devices to implement a new type of planar microassembly.

The remainder of this paper is organized as follows. Section II places our paper in the context of previous work. Section III reviews the operation of the stress-engineered MEMS microrobot, and Section IV describes the fabrication process for the microrobot species and addresses the issue of GA. Both Sections III and IV describe the innovations in MEMS design, fabrication, and engineering required to build our parallel controllable microrobots. Section V describes the designs and control strategies for independent microrobot species capable of microassembly. Experimental results from implementing microassembly using fabricated microrobots are presented in Section VI. Section VII discusses some of the limitations of the presented microassembly scheme, suggesting possible future work that can be used to overcome some of these shortcomings. Finally, Section VIII offers concluding discussion.

II. RELATED WORK

A. Microassembly

Microassembly is generally performed in one of two ways: robotic manipulation through the use of macroscale robotic manipulators with microscale end effectors [6], [7] or parallel self-assembly (SA), where structures are aggregated through stochastic interactions of components [8]–[11]. Robotic microassembly can exhibit high levels of accuracy; however, its acceleration and, thus, speed are often constrained by the additional mass of the manipulators (which is usually several orders of magnitude larger than the mass of the assembling components). To increase the efficiency of assembly without sacrificing its accuracy, parallel manufacturing architectures have been proposed, where large numbers of micro- or nanomachines assemble in parallel to form larger structures. For example, Popa and Stephanou [12] propose a multiscale approach, where tools and processes at different scales are combined in a single, parallel, bottom-up assembly architecture. This approach is similar to parallel molecular assembly proposed by Drexler [13]. One implementation of such parallel assembling is distributed manipulation [14]–[16], where arrays of micromanipulators are embedded into a surface (so-called *active surface*) and can be used independently to translate, orient, and assemble parts.

In contrast, SA [8]–[10] is a stochastic assembly process that does not have the resolution limitation of an active surface. The parts move at random, often through agitation without the use of external manipulators, and structures aggregate via mutually selective bonding. The geometry of the assemblies is programmed upon the fabrication of the individual components; concurrent control of the assembly process is, in general, not possible. Defect formation is also a common problem in SA

due to the local minima in the energy function, as reported by, e.g., Rothmund [10] and Winfree [17]. Approaches have been proposed to actively modulate the SA process [18], [19] to increase the yield. Specifically, Onoe *et al.* [18] reduced defect formation by introducing controlled sequential SA where one of the two types of adhesive surfaces was selectively activated during assembly.

In contrast to SA, our assembly scheme does not control the specific affinity between the individual components but rather the trajectories of the individual parts. Structure aggregation is promoted through intersecting trajectories. This allows our approach to generate a large variety of structures from the same set of components and to avoid the formation of defect assemblies through nonintersecting trajectories. Similar to SA, our scheme does not require external actuators to maneuver the assembling parts. The result is an efficient controllable assembly scheme with a yield that is comparable to robotic manipulation assembly and a footprint that is comparable to active surface assembly.

B. Microrobotics

The relative ease with which the snap-down and release voltages of the steering arms in the stress-engineered microrobots can be adjusted presents an unprecedented opportunity for the design and exploration of microscale multirobotic systems. Although there exist many MEMS-robotic systems, most previous works have involved layered designs that are composed of microfabricated components, with dimensions on the order of millimeters and centimeters [20], [21]. In such systems, which are also called *walking chips*, the vast majority of the mass of the robot is contained in its chassis. Powering MEMS robots without the use of restrictive wires or tethers is problematic, and onboard power generation is difficult due to the scaling laws as the size of the robot is further reduced. For example, the smallest robotic system with onboard power generation was developed by Hollar *et al.* [22]. The 8.5 mm × 4 mm solar-powered microrobot includes control circuits, power generation, and propulsion mechanism. In contrast, our microrobot [1] receives power that is necessary for its operation from the environment, using an untethered power-delivery scheme [2]. This allows the size of our robot to be almost two orders of magnitude smaller than the other previously developed systems.

Throughout this paper, we use the term *microrobot* to denote mobile untethered MEMS robots with their dimensions strictly confined within 1 mm³. In addition to implementing microassembly, micrometer-scaled robots are envisioned to be able to manipulate cells [23], explore unknown and potentially hazardous environments, or perform surveillance [24]. Yesin *et al.* [25] recently presented another microrobot that receives power through its environment; this 950- μ m-long microrobot is actuated using magnetic fields. This robot has interesting potential biomedical applications.

C. Multirobotic Systems and Control

Microscale multirobotic cooperation has not been previously attempted; however, there are many examples of macroscopic multirobotic systems that aggregate form or functionality

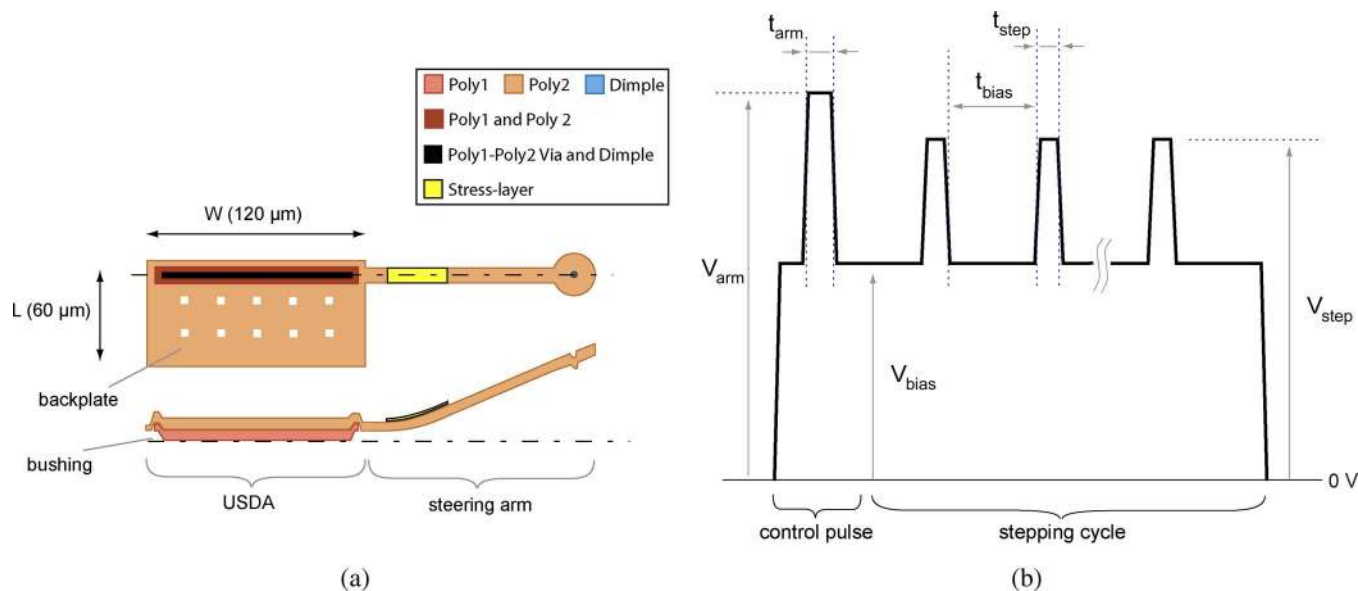


Fig. 4. Design of a stress-engineered electrostatic microrobot and its control and power-delivery signal. (a) The microrobot consists of an USDA, which is $120\ \mu\text{m} \times 60\ \mu\text{m}$, and a cantilevered steering arm with a circular pad at the end. A stress layer provides out-of-plane deflection of the steering arm. (b) The control and power-delivery signal consists of a control pulse V_{arm} and a stepping cycle containing up to 250 stepping pulses V_{step} . Voltage between the stepping pulses is kept at V_{bias} . After the stepping cycle, the polarity is reversed, and the waveform is repeated to prevent parasitic charging. Forty unbiased stepping pulses are then added to ensure that the steering arms always release from the substrate before beginning a new control and power-delivery cycle.

through cooperation or mutual interaction. Self-reconfigurable robot is an example of a robotic system composed of basic components that can reconfigure its shape and functionality [26], [27] to match the task at hand. Distributed algorithms and message-passing are used to control the reconfiguration process [28]. Decentralized cooperation of multirobotic systems can be achieved without the use of explicit communication. Rus *et al.* [29], Donald *et al.* [30], and Stilwell and Bay [31] show how implicit communication can be used to coordinate several robots to manipulate larger objects. Implicit communication has also been demonstrated by Pagello *et al.* [32] to control soccer robots in the Robocup competition. Decentralized coordination of microrobot motion can be also achieved through the use of local rules [33], [34]. However, most decentralized multirobotic control approaches assume that the robots have sufficient onboard hardware resources to receive and process sensory inputs and/or communicate with other devices. In contrast, our robots are much simpler and can only partially decode the broadcasted control signal. While the control of such systems has not been previously studied, the concept of selective response to a global control signal (*Global Control, Selective Response* [35]) is common in micro- or nanoscale biological systems; an excellent example is the embryogenesis of *Phylum Nematoda* [36]. A related theoretical motion planning approach for systems with limited individual controllability has been recently presented by Bretl [37], showing that it is possible to use the relative distribution of identical agents controlled through a global signal to perform useful tasks. Our work demonstrates that by designing microrobots that respond differently to a global control signal, we can control the robots to achieve microassembly. Furthermore, every theoretical idea introduced in our paper is experimentally tested, at least to proof-of-principle, by fabricating, controlling, and measuring the performance of these novel MEMS devices.

III. STRESS-ENGINEERED MEMS MICROROBOT

Fig. 4(a) shows an untethered stress-engineered MEMS microrobot used in this work. A detailed description can be found in [1]. The robot consists of an USDA [2] that provides forward motion and a curved steering-arm actuator that determines whether the robot moves straight or turns. The robot moves similarly to a Dubins car [38] that can only turn in one direction and can only move forward. The robot is globally controllable (shown in [1]), but it is not *small-time locally controllable*² (STLC), restricting its ability to operate in the presence of obstacles. Its configuration is defined as the vector $q = (x, y, \theta)^T$, and its velocity is $\dot{q} = \nu(\sin \theta, \cos \theta, ah/r)^T$, where $h \in \{-1, 1\}$ and denotes whether the steering arm is on the right or the left side, ν is the velocity of the SDA, r is the turning radius, and $a \in \{0, 1\}$ is the state of the steering arm ($0 = \text{up}, 1 = \text{down}$).

The steering-arm actuator consists of a cantilever beam with a circular pad and a $0.75\text{--}1.2\text{-}\mu\text{m}$ -deep dimple to prevent irreversible stiction. The microrobot operates on a grid of zirconia-insulated interdigitated electrodes. When voltage is applied between sets of electrodes, the electrodes and the conductive chassis of the microrobot form a capacitive circuit, and an electric potential is induced on the microrobot. This potential causes the microrobot body to be attracted to the electrode field, and the scratch-drive converts this vertical motion into a forward step.

The interdigitated electrodes are used both to provide power to the microrobot by actuating the scratch drive and to control the microrobot motion through the actuation of the steering arm. Fig. 4(b) shows the control and power-delivery signal that is applied to the microrobot during operation. The first part of the signal consists of a single control pulse of duration t_{arm}

²See Appendix. Definition of Terms.

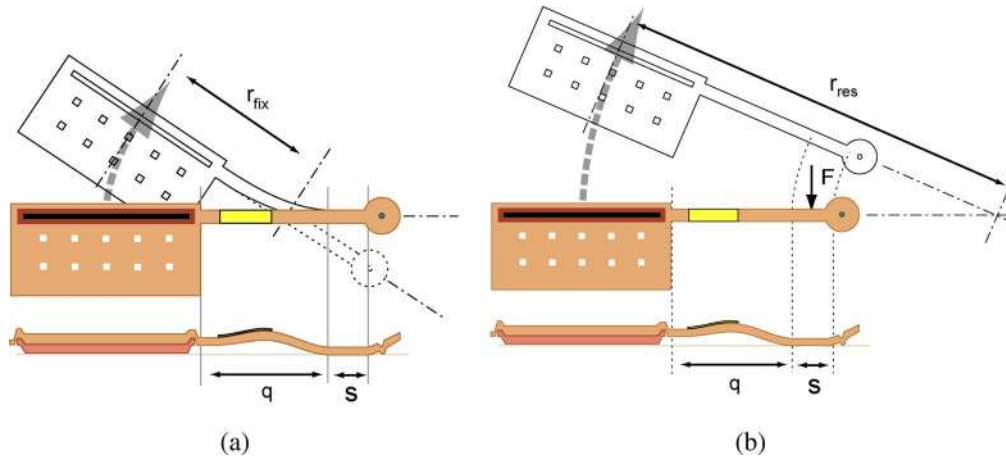


Fig. 5. Turning mechanisms of the stress-engineered microrobot. (a) During fixed-contact turning, a segment s of the steering arm remains in a fixed contact with the substrate. During the stepping cycle, the microrobot flexes the suspended portion of the arm q while turning around radius r_{fix} . This mechanism produces turning radii that are smaller than the length of the steering-arm actuators. (b) During resistive-contact turning, the segment of the arm in contact with the substrate provides a resistive force which induces a moment on the microrobot, making it turn. Resistive-contact turning produces turning radii that are larger than the length of the steering-arm actuators.

applying voltage V_{arm} to the microrobot. If the snap-down transition voltage (V_{down}) of the steering arm is lower than V_{arm} , the arm is pulled down in contact with the substrate. For the microrobots presented in this paper, V_{arm} ranges between 140 and 220 V, and t_{arm} is typically 460 μs . Following the control pulse, a stepping cycle consisting of 250 stepping pulses is applied. Each pulse causes the SDA to move forward [only three stepping pulses are shown in Fig. 4(b)]. The voltage used for the stepping pulses alternates between V_{step} and V_{bias} . To power microrobots presented in this paper, V_{step} is nominally 130–140 V, and t_{step} is 370 μs . The peak of each stepping pulse causes the backplate of the SDA to flex. When the voltage recedes down to V_{bias} , the flexure in the backplate is relaxed, and the SDA steps forward [39]. If V_{bias} recedes below the release transition voltage of the steering arm (V_{up}), the arm is released from the substrate. In our system, V_{bias} varies from 100 to 0 V, and t_{bias} is typically 1.5 ms. After completion of the stepping cycle, the polarity of the waveform is reversed, and the signal is repeated. The polarity reversal and the low duty cycle (20%) of the stepping pulses help relieve parasitic charging that otherwise would accumulate during operation. After the reversed polarity stepping cycle, 40 unbiased stepping pulses are added to ensure that the steering arms always release from the substrate before beginning a new control and power-delivery cycle. The entire voltage sequence is then repeated.

A. Turning

The state of the steering-arm actuator determines whether each robot moves straight or turns. Turning behavior is always initiated by snapping down the steering arm using a control pulse with a higher voltage than the snap-down voltage (V_{down}) of the respective steering arm. During the application of the stepping pulses, V_{bias} remains above the release voltage of the steering arm, such that the arm remains down through the entire stepping cycle. A portion of the arm will remain in flat contact with the substrate. The application of the stepping pulses causes the microrobot to move forward; however, its motion is restricted by the portion of the arm that is snapped-down,

causing the robot to follow a curved trajectory. Two distinct mechanisms, which are differentiated through the design of the steering arm, are responsible for microrobot turning. These are the *fixed-contact turning* and the *resistive-contact turning*.

The fixed-contact turning mechanism is shown in Fig. 5(a). During the fixed-contact turning, the portion of the steering arm that is pulled in contact with the substrate, s , remains fixed. The robot induces a flexure in the suspended portion of the arm q , causing it to turn. At the end of the 250 stepping pulses, the waveform polarity is reversed, and V_{bias} transitions through 0 V, releasing the arm. The flexure is relieved, and a new turning cycle begins with the application of another control pulse. This turning behavior is most commonly observed in devices with small steering-arm pads and long steering-arm beams. A characteristic of this turning mechanism is a turning radius that is smaller than the length of the steering arm.

Fig. 5(b) shows the resistive-contact turning mechanism, which is most common in devices with large steering-arm pads. In this mechanism, the microrobot turns through frictional contact between the flat portion of the arm and the substrate. The part of the arm in contact with the substrate provides frictional resistive force F that, in turn, induces a moment on the SDA, causing it to turn. This mechanism results in turning radii that are greater than the length of the steering-arm actuators.

Fixed-contact turning can be viewed as a special case of resistive-contact turning, using static as opposed to dynamic friction. Empirical data suggest a distinct separation between the two mechanisms rather than a gradual reduction in radii of curvature as we transition from resistive to fixed-contact turning. This is consistent with our observations of a much larger static than dynamic friction component.

The selection of the turning mechanism depends on the design of the steering-arm actuator and on the voltage levels of the control and power-delivery signal. A bias voltage close to the release voltage of the steering arm tends to engage resistive-contact turning. Out of five microrobot species presented in this paper, species 1, 3, and 5 exhibit mostly fixed-contact turning. Species 2 and 4 have large pads and typically exhibit resistive-contact turning.

IV. FABRICATION

We have fabricated and tested 15 microrobots, conducting three independent stress-engineering deposition runs on each of the five microrobot species. Single-device trimming was used to adjust the steering-arm transition voltages of one device from species 2 and one device from species 5. However, damage to the device from species 2 (caused by arcing due to dielectric breakdown) prevented us from fully completing the adjustment, reducing the number of operational devices to 14.

The fabrication of the microrobot chassis is performed through the surface micromachining PolyMUMPS foundry process [4]. The chassis is formed from the top layer of polysilicon, which is referred to as the Poly2 layer, whereas the bushing is formed from both the Poly1 and Poly2 layers. The design of a generic microrobot is shown in Fig. 4(a). In all our microrobot species, the USDA is composed of a $120\ \mu\text{m} \times 60\ \mu\text{m}$ backplate and a $1.5\text{-}\mu\text{m}$ -tall bushing. The steering arms vary in length from 120 to $160\ \mu\text{m}$, the diameter of the pad ranges from 20 to $40\ \mu\text{m}$, the width of the cantilever beam is either 8 or $10\ \mu\text{m}$, and the dimple is either 0.75 or $1.2\ \mu\text{m}$ deep.

After the PolyMUMPS process is complete, a portion of each arm is coated with evaporated chromium (stress engineering). The tensile residual stress of the chrome layer curves the steering arms upward and is one of the factors determining their transition voltages. In the infrequent cases when compounding process variability due to GA or other factors causes the transition voltage of the steering arms to deviate significantly from their design, a post-release trimming method can be used to further increase or decrease the curvature of the individual steering arms.

Once fabrication of both the microrobots and the operating environment is completed, the devices are transferred in batches from the die to their operating environment using a structure we call a *transfer frame*. The position of individual devices can be further adjusted using a vacuum microprobe.

The operating environment for the microrobots consists of zirconia-insulated interdigitated electrodes. The electrodes are composed of a $500\text{-}\text{\AA}$ gold layer, which is patterned through a liftoff process. They reside on a silicon substrate, which is covered with a $3\text{-}\mu\text{m}$ -thick layer of thermal silicon oxide. The electrodes are coated with $0.5\ \mu\text{m}$ of reactive-evaporated zirconium dioxide, which is followed by a $300\text{-}\text{\AA}$ passivation layer of evaporated silica. A more detailed description of the fabrication process for the operating environments is given in [1].

A. Stress Engineering

The microrobots are received from the foundry on a 1-cm^2 silicon die. After the protective photoresist is removed, the die is soaked for a short time in buffered hydrofluoric acid (BHF), underetching the top polysilicon layer. This underetching produces a reentrant profile that is subsequently used to define the area of chrome covering the steering arm. Two consecutive baths are used to perform the BHF soak, and the die spends an equal amount of time in each bath. We have found that this greatly reduces the effects of GA on the polysilicon structures. After rinsing and drying, the die is coated with $76\text{--}96\ \text{nm}$ of thermally-evaporated chromium. The deposited chrome has an

intrinsic tensile residual stress, which produces the necessary curvature of the steering arms. The chrome is then lithographically patterned using a perchloric-acid-based chrome etchant.

Once the chrome pattern has been defined, the microrobots are released through a soak in 49% HF. A double bath system is again used. After rinsing in deionized water, the die is dehydrated by soaking in isopropyl alcohol and transferred to an ozone-friendly fluorocarbon solvent (based on 2,3-dihydrodecafluoropropentane and isopropanol). After a 25-min soak, the die is dried by a slow removal from the solvent, which is followed by a 3-min bake on a $120\text{-}^\circ\text{C}$ hotplate.

B. Transfer Frames

The microrobots are fabricated and attached to larger structures called *transfer frames* (Fig. 6), which are used to transfer multiple devices between the die and the operating environment. The relative position of our devices is set in design, and the attached transfer frame allows us to move this entire configuration to the operating environment. Fig. 6(a) shows an optical micrograph of a transfer frame. Microrobots are fabricated attached to the transfer frames through notched sacrificial beams, as described in [2]. Mechanical hinges are placed around the perimeter of the frame, enabling the manipulation of the frame using conventional microprobes. Once a transfer frame is placed on the designated operating environment, mechanical pressure, such as provided through a microprobe or electrostatic pull-down to the operating environment, is used to immobilize one or more microrobots. The transfer frame is then lifted, severing the sacrificial beams [Fig. 6(b)]. After the mechanical pressure is removed, the microrobots remain on the electrode grid. It may be possible to automate the manual release of the devices through an electromechanical self-release mechanism, such that all robots are released simultaneously. We presented a proof-of-concept planar self-release mechanism in [2]. Although the transfer frame represents a batch-transfer mechanism, any nonconforming devices must be individually discarded or moved for rework via postrelease trimming (see Section IV-D) using a vacuum microprobe.

C. Galvanic Attack

Undesired electrogalvanic effects, which are commonly called *galvanic attack* (GA), can cause degradation of polysilicon structures during release in HF [40]–[42]. Tocheux *et al.* [43] reported an accelerated degradation of polysilicon structures in buffered HF solution. Stress-engineered MEMS microrobots are highly susceptible to GA degradation because the underetch bath exposes polysilicon structures to BHF prior to chrome deposition, and the release etch exposes the polysilicon structures to HF in the presence of metal from the stress-inducing layer. Both the BHF and HF exposures in the presence of metal have been shown to promote GA and the corresponding polysilicon degradation. The effects of GA are often localized and can result in scorching, namely, dark and granular silicon surfaces, as well as variations in the thickness of the polysilicon structures. We found that poor chrome adhesion during the release etch is correlated with such polysilicon scorching. This could be caused by oxide growth

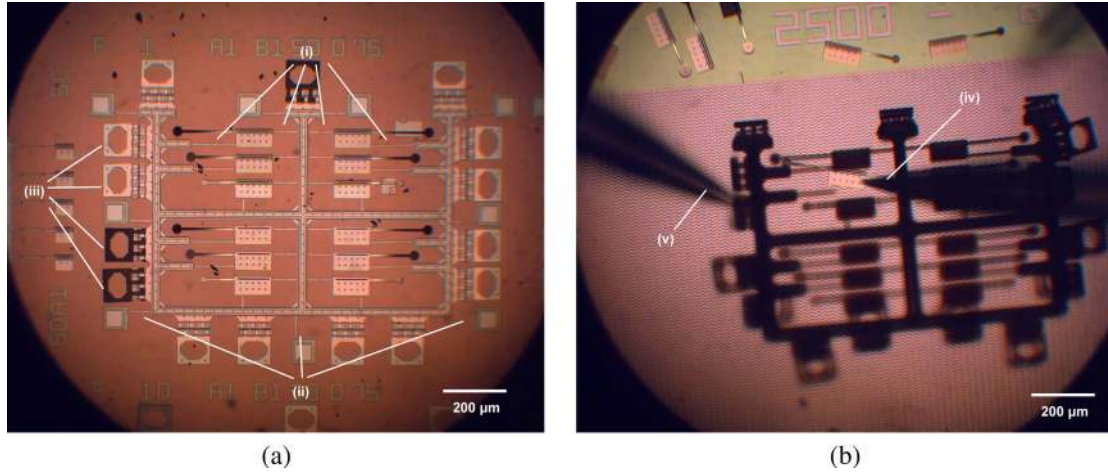


Fig. 6. Optical micrograph of a batch transfer structure called a *transfer frame*. (a) Microrobots are manufactured connected to the frame through sacrificial notched beams (i). The frame is anchored to the substrate through another set of sacrificial beams (ii). These beams are broken, and the frame is lifted of the substrate by microprobes inserted into hinged ears at the perimeter of the frame or using a vacuum microprobe (iii). (b) Once a transfer frame is placed on the destination operating environment, mechanical pressure, such as provided through a microprobe (iv), is used to immobilize the microrobots. The transfer frame is then lifted, for example, using a second microprobe (v), severing the sacrificial beams connecting the robots to the frame.

on the polysilicon surface [42] prior to chrome deposition. We have also measured significant thinning of polysilicon structures on die with visible GA scorching. In some cases, the structure thickness was degraded by up to 100 nm.

We observed GA effects on die containing gold features; however, gold is not electrically connected to the structures that are attacked. Our use of a double-bath BHF and HF soak, which is described earlier, has eliminated the occurrence of visible GA scorching and the chrome adherence problems. However, the variability in radii of curvature suggests that some structural thinning may still exist.

Structural thinning has a significant impact on the transition voltages of the microrobot steering arms. Consider Stoney's equation [44], which can be used to estimate the amount of curvature produced through a stress-engineering process

$$\rho = \frac{E_s t_s^2}{6 t_f \sigma_f}. \quad (1)$$

Here, ρ is the radius of curvature, σ_f is the film stress, t_s is the thickness of the steering arm, and t_f is the thickness of the film. Equation (1) assumes that $t_s \gg t_f$, which is the case in our stress-engineered microrobots. We note that ρ scales with t_s squared (t_s^2).

For an initial thickness of 1.5 μm and a structural thinning of 1000 \AA , ρ decreases from 800 to 700 μm . This would change the deflection of a 120- μm -long chrome-covered beam by 1.27 μm . Such a change in tip deflection is sufficient to significantly alter the transition voltage of the steering arm. Out of five microrobot species presented in this paper, species 5, which contains the longest steering arm, is most sensitive to GA-induced changes in the radius of curvature.

D. Post-release Trimming

Post-release trimming can be applied to correct for deviations in the deflection of the steering-arm actuators from the combined process variability caused by GA or other factors. It uses a prefabricated fixture that immobilizes a released microrobot,

such that additional chrome can be deposited on its steering arm. Chrome is deposited on the top surface of the arm to increase the curvature or on the bottom surface of the arm to decrease it. Fig. 7(a) shows an idealized schematic representing the support fixture used for postrelease trimming. The fixture is anchored to a handle substrate through a linear spring that provides a normal force immobilizing the microrobot. The handle substrate is subsequently placed in a thermal evaporator for additional chrome deposition. The fixture also functions as a shadow mask, limiting the chrome deposition to the surface of the steering-arm actuator.

Stoney's equation (1) can be used to estimate the amount of additional chrome to be deposited on the steering arm in order to achieve the desired deflection. The accuracy of such estimates is limited by nonlinear effects in the stress of the deposited chrome, as well as the difficulty of precisely defining the exposed region during additional chrome deposition. However, post-release trimming can be applied multiple times on the same microrobot, and thus, an iterative approach can be used to precisely tune the transition voltage of the steering arm.

We used a PolyMUMPS die as a handle substrate and a SDA attached to a transfer frame as a support fixture. Top part of Fig. 7(b) shows a microrobot from species 2 protruding from the scratch drive used as the support fixture. A portion of the scratch-drive backplate was exposed during chrome deposition; hence, the discoloring is visible in bottom part of Fig. 7(b). Table I shows the effect of postrelease trimming of two devices: a device from species 2 and a device from species 5. The table shows the amount of chrome deposited on the top or bottom of the steering arm, the corresponding change in tip deflection, and the observed change to the transition voltage of the steering arm.

V. PARALLEL CONTROL FOR MICROASSEMBLY

A group of our microrobots is both nonholonomic and highly underactuated; the single global control and power-delivery signal causes all microrobots to move at the same time. Because all

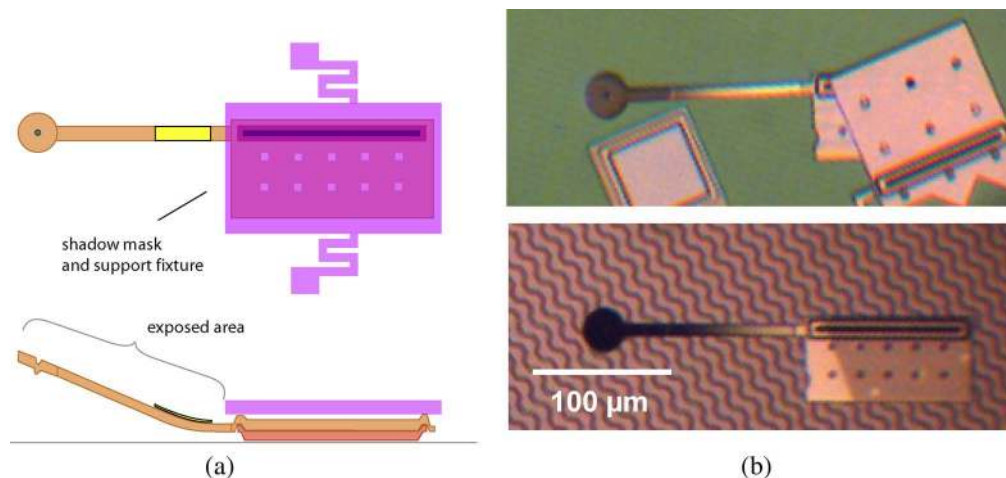


Fig. 7. Post-release trimming method used to adjust the transition voltages of the steering-arm actuators. (a) Schematic illustration of the support fixture that is used to immobilize the microrobot and provide a shadow mask restricting the chrome deposition to the steering arm. (b) Optical micrograph showing (top) a microrobot belonging to species 5 immobilized on a PolyMUMPS die in preparation for additional chrome deposition and (bottom) the same microrobot on the operating environment after the trimming operation. Discoloring of the scratch-drive backplate due to the incomplete coverage of the shadow mask is visible; such backplate chrome has only marginal impact on the walking behavior of the SDA.

TABLE I
IMPLEMENTATION OF SINGLE-DEVICE TRIMMING

Device	Additional Cr thickness	Tip deflection Δ	Transition voltage before trim	Transition voltage after trim
species 5	160 Å (Top)	4.4 μm	$V_{\text{down}} = 170 \text{ V}$	$V_{\text{down}} = 195 \text{ V}$
species 2	80 Å (Bottom)	-3 μm	$V_{\text{up}} = 90 \text{ V}$	$V_{\text{up}} = 75 \text{ V}$

devices move in parallel, the control of such a system is much more difficult than in the case of a single robot [1]. We show that if each of the robot steering arms has a unique pair of snap-down and release voltages [i.e., either V_{down} or V_{up} must differ between any two robots, see eq. (2)], then the robots belong to independent microrobot species, and when implementing microassembly, we can transform the task of simultaneously controlling n microrobots to simultaneous control of *two* robots, followed by sequential control of *single* devices. The control scheme presented in this section consists of a general motion planning technique for pairs of robots and single robots, coupled with a heuristic approach to correct for control error. This control scheme, although not completely general, was sufficient to achieve precise microassembly using our microrobots.

We first define a few basic concepts. The curved and straight motion segments, which the robot's trajectory is composed of, are called *motion primitives*. For example, a turn-straight-turn trajectory is composed of three motion primitives. The motion primitives are activated using distinct control and power-delivery waveforms. Each such waveform is specified through h successive V_{arm} values (corresponding to h control pulses, $h \geq 1$), followed by V_{step} and V_{bias} , and is called a *control primitive*. To address the steering arms of n microrobots, a control primitive might contain up to $2n$ control pulses. A *control sequence* is a sequence of control primitives specifying a trajectory for the microrobots from some initial configuration. Each control primitive is applied for a specific duration of time, and the timing duration is included in the control sequence. For example, a control sequence S consisting of two control primitives, namely, A and B, applied for 10 and 20 s, respectively, is written as $S = \{A_{10}, B_{20}\}$.

Consider a system composed of n microrobots. The configuration of such a system can be described as a vector $\mathbf{q} = (q_1, q_2, \dots, q_n)$ of configurations q_i of the individual robots. The problem of controlling n microrobots can be formalized as finding and applying a control sequence S , such that \mathbf{q} enters the goal region G from any set of initial configurations R . We use regions as opposed to single-point configurations to reflect the uncertainty in measuring the robots' position. R is a ball in C-space, whereas G is a small open set about some assembled configuration. To account for control error, a *control strategy* executes S while periodically sensing the position of the robots and modifying S to correct for the control error. In our case, the control strategy is implemented through a closed-loop control algorithm. This algorithm signals success, i.e., *terminates*, when \mathbf{q} enters G .

For i^{th} microrobot, let V_{down}^i be its snap-down voltage, and let V_{up}^i be its release voltage. The robots belong to independent microrobot species if

$$(V_{\text{down}}^i, V_{\text{up}}^i) \neq (V_{\text{down}}^j, V_{\text{up}}^j), \quad i, j \in \{1, \dots, n\}, i \neq j. \quad (2)$$

The voltage levels of the control and power-delivery signal are ultimately bounded by the breakdown voltage of the ZrO_2 electrode insulator. Adequate separation must be maintained between the transition voltages, such that the steering arms can be actuated separately despite the inherent variation in the fabrication process and the power coupling to the robot chassis. We call such transition voltages *significantly different*. In our system, we maintained a minimum 30 V gap between the control voltage levels of the control signal to ensure individual addressing of the steering arms for the independent microrobot species. Let k be the number of significantly different snap-down

TABLE II
EXAMPLE CONTROL MATRIX FOR $n = 2$ MICROROBOT SYSTEM

Control Primitive	Robot 1	Robot 2
A	T	T
B	T	S
C	S	S

voltages, and let ℓ be the number of significantly different release voltages. It can be shown that the number of independently controllable microrobots is bounded by the product $k\ell$.

There are other constraints that must be satisfied to assure proper operation of the microrobots during all the control primitives. The separation between V_{step} and V_{bias} in each control primitive must be sufficient to allow the scratch drive to flex and relax, producing forward motion. Furthermore, if the snap-down voltage of a steering arm (V_{down}) is lower than V_{step} , then only the release voltage (V_{up}^i) can be used to control the robot operation. In such a case, V_{up}^i must be unique. However, V_{up}^i must be lower than V_{bias}^i of at least one of the control primitives in order for the robot to be able to turn.

The behavior of a group of microrobots is summarized in a *control matrix*. An example of a control matrix for two devices and three control primitives is shown in Table II. Rows correspond to control primitives and are sorted in the decreasing order of V_{arm} and V_{bias} . The columns of the matrix correspond to the robots and are sorted in the order of increasing transition voltage of the steering arms. The individual cells denote the behavior of microrobot j during the application of control primitive i . We denote the turning behavior as **T** and the straight motion as **S**. The cells denoting turning behavior are shaded to outline the structure of the control matrix.

The control strategy for n microrobots requires $n + 1$ control primitives and a control matrix of size $n(n + 1)$. The matrix is not square; however, if we define the diagonal elements as $(i, i) : i \in \{1 \dots n\}$, then the diagonal and the cells above it specify turning behavior only, forming an upper triangular (UT) matrix. Cells representing the straight motion form a lower triangular (LT) matrix below the diagonal.

A. Designs of Independent Microrobot Species

We designed and fabricated five microrobot species using three separate stress-engineering runs. Four of the species are designed to be independent, i.e., satisfy eq. (2). The steering arms in all the five species are fabricated out of 1.5- μm -thick polysilicon layer. Table III summarizes the design parameters for the steering arms defining each of the species. An annotated design of the steering arm is shown in Fig. 8 to provide a reference for the parameters in Table III. The layer of evaporated chrome is 76 nm thick, except for species 5 where the nominal thickness of chrome ranges from 76 to 92 nm to compensate for design-specific local effects of GA. The steering-arm designs were determined based on closed-form equations [1], finite-element models, and empirical data, such that their transition voltages are reproducibly confined to the voltage ranges shown in Table IV.

The nominal stepping voltage of all control primitives is 140 V, which is above the snap-down voltage of species 1 and 2.

Consequently, species 1 and 2 must use unique release transition voltage (V_{up}) ranges for the purpose of control. Species 3 is assigned a unique V_{up} range, whereas species 4 and 5 are assigned unique snap-down transition voltage (V_{down}) ranges. The waveforms of the corresponding five control primitives that are used to control the system are shown in Fig. 9. The primitives are labeled A–E according to the decreasing order of their V_{arm} and V_{bias} voltages.

The control matrix for the five microrobot species is presented in Table V, where each cell denotes the behavior of species j during control primitive i , **T** denotes turning, and **S** denotes straight motion. Cells with turning behavior are shaded. Each cell also contains experimentally-measured parameters characterizing the motion of the microrobots under each control primitive. Radii of curvature larger than 550 μm are categorized as straight motion, and radii of curvature larger than 2000 μm were not measured. The data represent average behavior across three independently-fabricated devices for each species, except for data from species 2 which contain averages across two independently-fabricated devices. The control matrix for the four independent microrobot species, i.e., devices 1, 3, 4, and 5 or 2, 3, 4, and 5, is composed of a UT matrix containing cells with turning behavior and an LT matrix containing cells denoting forward motion. A control matrix of this form allows us to use the control strategy described in Section V-B (below) to implement microassembly.

Experimentally-measured trajectories of the microrobots during the application of each control primitive are shown in Fig. 10. For each control primitive, two trajectories are shown for each stress-engineering run of each microrobot species. A total of 140 such trajectories are shown, with 28 tracks for each of the five control primitives. Panels (a)–(e) show how the microrobot species progressively switch from turning to straight-line motion as control primitives with progressively lower transition voltages are applied.

B. Control Strategies for Microassembly

We implement microassembly using the structure of the control matrix to transform parallel control of n independent species of microrobots to parallel control of two devices, followed by sequential control of single robots. This section considers only *nominal* (error free) microrobot trajectories and can be viewed as geometric motion planning [45]. Methods for correcting the inherent variability of microrobot motion, called *control error*, will be discussed in Section V-C. We assume that all the robots move with equal velocities.

To ensure stability of the intermediate assemblies, we restrict the structures that can be assembled to those that can be reached via the progressive assembly of *compliant-stable structures*. Compliant-stable structures do not change their configuration while the devices are powered; the sum of forces (including friction) and moments, which are generated by all the robots and transmitted through compliant interaction, is equal to zero. The structures shown in Fig. 3 are compliant-stable for most of the control primitives in the Table V control matrix.

Consider a system of n microrobots (devices) D_i , $i \in \{1, \dots, n\}$, labeled according to the increasing transition

TABLE III
DESIGN PARAMETERS FOR THE STEERING ARMS FOR MICROROBOT SPECIES 1–5

Species	Arm-orientation	D [μm]	w [μm]	L [μm]	L_c [μm]	L_o [μm]	Dimple height [μm]
1	left side	20	10	120	33.5	9.5	0.75
2	left side	40	8	80	59.5	9.5	1.2
3	right side	20	10	120	33.5	1.5	0.75
4	right side	36	8	107	94.5	1.5	0.75
5	left side	30	8	130	91.5	1.5	0.75

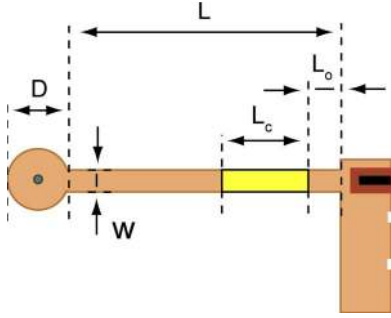


Fig. 8. Parameters of the steering arms specified in Table III classifying the five microrobot species.

TABLE IV
RANGES OF TRANSITION VOLTAGES FOR MICROROBOT SPECIES 1–5

Species	Snap-down Voltage (V_{down})	Release Voltage (V_{up})
1 & 2	below 140 V	below 65 (± 5) V
3	below 160 V	65 - 95 (± 5) V
4	160 - 190 V	below 95 (± 5) V
5	above 190 V	below 95 (± 5) V

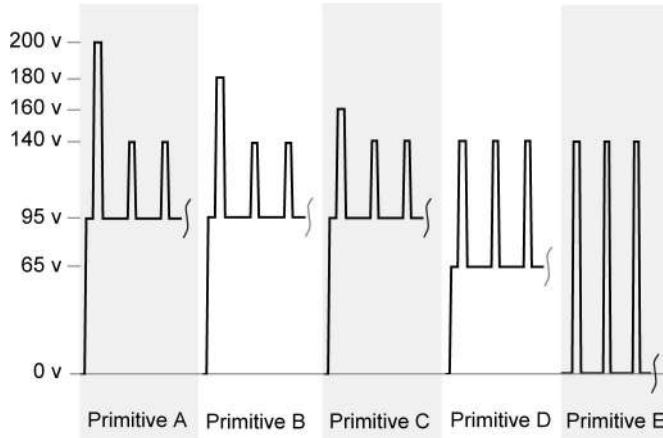


Fig. 9. Waveforms (control pulse and two stepping pulses only) of the five control primitives used to control the five microrobot species described in Table III. Average V_{arm} , V_{step} , and V_{bias} voltage levels are shown. The actual voltage levels used to control the individual groups of microrobots could vary by up to ± 10 V.

voltages, and a corresponding control matrix M containing $n + 1$ control primitives P_j , $j \in \{1, \dots, n + 1\}$, labeled according to the decreasing number of turning devices. The assembly takes $n - 1$ steps. In step 1, we assemble the initial stable shape G_1 using two simultaneously-controlled microrobots. In steps $2, \dots, n - 1$, the goal shape is progressively assembled through sequential addition of single robots while maintaining the stability of the accumulating structure.

Step 1. Assembly of the Initial Stable Shape: The initial stable shape is assembled through simultaneous control of robots D_n and D_{n-1} using control primitives P_1 , P_2 , and P_3 .

Regardless which of these primitives is applied to the system, D_{n-2}, \dots, D_1 orbit in circular trajectories. A two-stage control strategy assembling the initial stable shape is shown in Fig. 11. During the first stage, D_n is maneuvered to an intermediate configuration (label (iv) in Fig. 11) using primitives P_1 and P_2 , whereas D_{n-1} orbits. During the second stage, D_{n-1} is maneuvered to its target location to dock with D_n (ii) using primitives P_2 and P_3 . P_2 and P_3 cause only a straight-line motion of D_n . Consequently, the intermediate configuration (iv) must be a configuration from which D_n can dock with D_{n-1} (iii) through a straight-line trajectory (v) that is equal in length to the trajectory of D_{n-1} in stage 2.

This strategy allows us to control the position and orientation of the initial stable shape and, consequently, the final assembly; however, it requires sufficiently large space to accommodate the straight-line motion of D_n during the second stage. This space requirement can be conservatively bounded by $\pi(s + 2r + w)^2$, where s is the length of the longest trajectory of D_n or D_{n-1} to reach the docked position in isolation, r is the turning radius of the robot, and w is the width of the SDA ($s \gg r, w$). This space requirement can be further reduced by relaxing the position and orientation of the initial stable shape [position and orientation of (ii) and (iii)] by simply directing the microrobots to the closest intersecting point of their trajectories.

Steps 2, ..., n - 1. Subsequent Addition of Single Robots: Once the initial stable shape is assembled, single microrobots are added in a way that maintains the stability of the accumulating structure. The robots are added in the order of $D_{n-2}, D_{n-3}, \dots, D_1$ using the pairs of control primitives (P_3, P_4) , $(P_4, P_5), \dots, (P_n, P_{n+1})$. Primitive pair (P_3, P_4) provides turning and straight-line motion to robot D_{n-2} , while D_{n-3}, \dots, D_1 orbit, and D_{n-1}, D_n are immobilized in the assembling structure. After docking robot D_{n-2} , primitives (P_4, P_5) are used to control robot D_{n-3} and so on. The assembly is completed after $n - 1$ stages.

Initial Configuration Requirements: To achieve successful microassembly, the initial positions of the microrobots must be sufficiently separated to prevent collisions between the orbiting devices. Furthermore, there must be enough space to allow the assembly of the initial stable shape and to allow single devices to be maneuvered to dock with the assembling structure. The separation between the orbiting robots must also be able to accommodate a small drift of their orbits due to accumulating control error.

C. Error Correction

We apply error detection and recovery (EDR) and preimage approach [46], [47] to extend motion planning from Section V

TABLE V
CONTROL MATRIX FOR THE FIVE MICROROBOT SPECIES. T DENOTES TURNING, AND S DENOTES STRAIGHT-LINE MOTION. THE NUMBERS REPRESENT AVERAGE LINEAR VELOCITY (LEFT, IN $\mu\text{m/s}$) AND RADIUS OF CURVATURE (RIGHT, IN μm), MEASURED EXPERIMENTALLY. STANDARD DEVIATION ACROSS INDEPENDENT FABRICATION RUNS IS REPORTED IN PARENTHESIS ON THE RIGHT SIDE OF THE AVERAGES

C.P.	Species 1	Species 2	Species 3	Species 4	Species 5
A	13 (4) T 158 (7)	16 (1) T 202 (32)	17 (1) T 210 (32)	17 (2) T 316 (92)	13 (3) T 167 (14)
B	12 (5) T 160 (4)	13 (2) T 195 (42)	18 (1) T 195 (23)	18 (2) T 322 (112)	18 (1) S 1990 (17)
C	14 (1) T 157 (1)	17 (0) T 227 (8)	18 (4) T 172 (7)	21 (7) S >2000 (na)	14 (1) S 1406 (595)
D	19 (1) T 211 (43)	17 (5) T 273 (3)	21 (3) S 1650 (606)	16 (5) S 1549 (373)	16 (3) S 1720 (484)
E	16 (2) S 1699 (384)	14 (1) S >2000 (na)	17 (2) S 1570 (720)	14 (1) S 1457 (742)	15 (4) S >2000 (na)

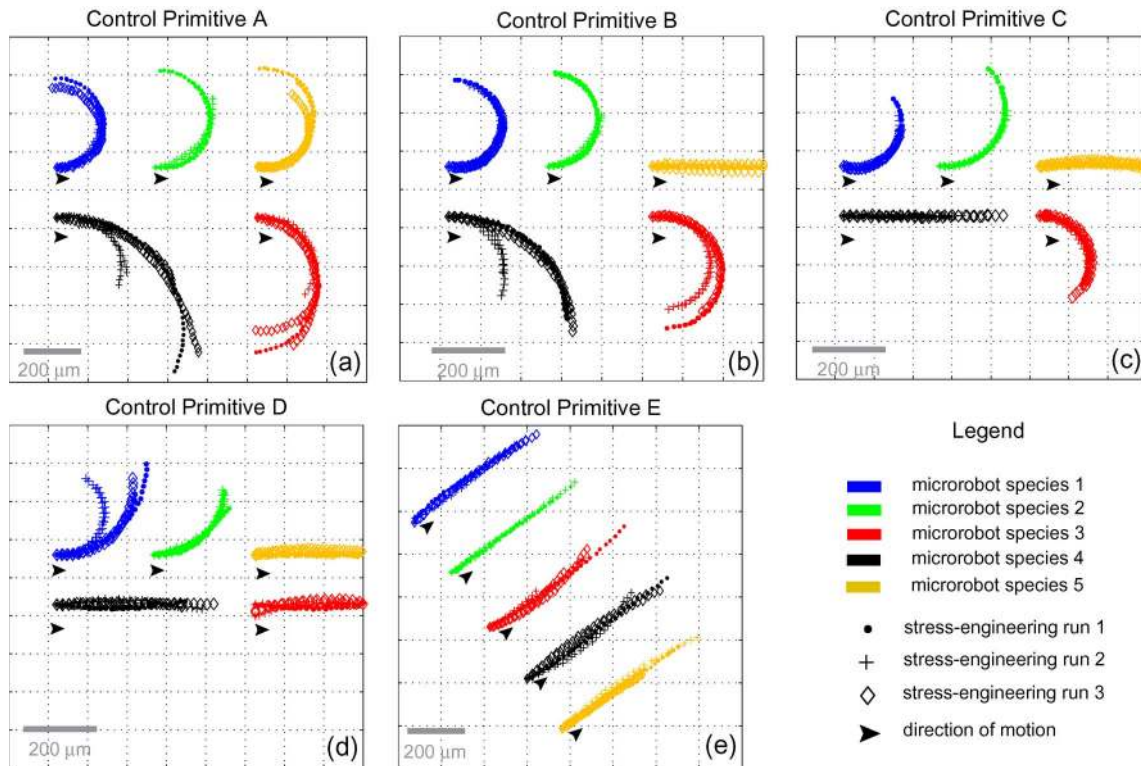


Fig. 10. Tracks showing the reproducibility of motion of the microrobot species during the application of the control primitives. Each track represents a single independent experiment. In particular, a total of 140 tracks are shown, with 28 tracks for each of the five control primitives. For each of the device species, two tracks are shown for each of the robots fabricated through independent stress-engineering runs. The species 1, 2, and 5 are left-handed; hence, they turn counterclockwise. The species 3 and 4 are right-handed and turn clockwise. Species 4 and 5 show a slight tendency to turn in the opposite direction of their steering arms when the arms are elevated; however, in all cases, the radii of curvature are larger than $550 \mu\text{m}$.

to construct heuristic control strategies that include online error correction. Let us first consider error correction for trajectories of single microrobots. We divide the trajectory of a single robot into two parts. In the first part, the robot is maneuvered to a *preimage configuration* (for example, (iv) in Fig. 13.) A preimage configuration is a configuration within the *strong preimage*³ (from which the robot is guaranteed to reach the goal) of the target docking configuration. This implies that a control strategy (*preimage control strategy*) can be constructed, allowing sufficient error correction for the robot to reliably enter the goal (via a *preimage trajectory*). In the second part of its trajectory, the robot follows the preimage trajectory to its docking configuration with a stable structure.

Error correction in the first part of the trajectory execution is performed by periodically recalculating the trajectory to ac-

count for deviations due to control error. Error correction during the second part of the trajectory execution is performed through online adjustments to the preimage trajectory. The preimage trajectory consists of interleaved straight and curved trajectory segments, and control error correction is performed by adjusting their ratio. Compliant interaction of the docking microrobot with the stable shape enhances our ability to achieve precise assemblies, as it significantly enlarges the preimage of the docking configuration. The front edge of the robot aligns perfectly with the straight edge of the stable shape, allowing the incident angle of the docking robot to vary by up to $\pm 45^\circ$ (conservatively estimated). This allows us to sacrifice the control of the incident angle for the docking robot in favor of the precise control of its docking location. Optimal error correction is possible when the target docking configuration is located in the middle of the *error-correction cone* [Fig. 12(a)], which is spanned by full-turning and straight-line motion trajectories. Fig. 12(a) shows the preimage trajectory (i) and the error-correction

³See Appendix. Definition of Terms.

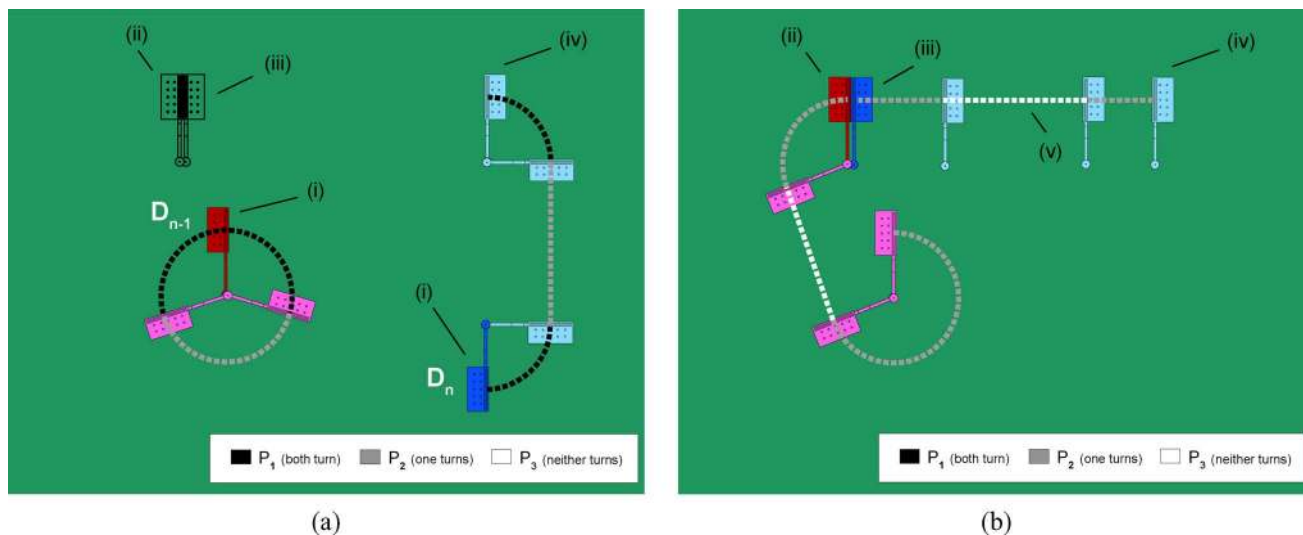


Fig. 11. Illustration of the two-stage control strategy for the assembly of the initial stable shape. Robots D_n and D_{n-1} are colored blue and red, respectively. Dark blue and red denote the initial (i) and target configurations (ii, iii). The color of the track represents the control primitives that are used to generate the respective motion. (a) In stage 1, D_n is maneuvered to an intermediate goal configuration (iv), whereas D_{n-1} orbits. (b) In stage 2, D_{n-1} is maneuvered to its target configuration (ii), whereas D_n moves along a straight-line trajectory (v) into its target configuration (iii).

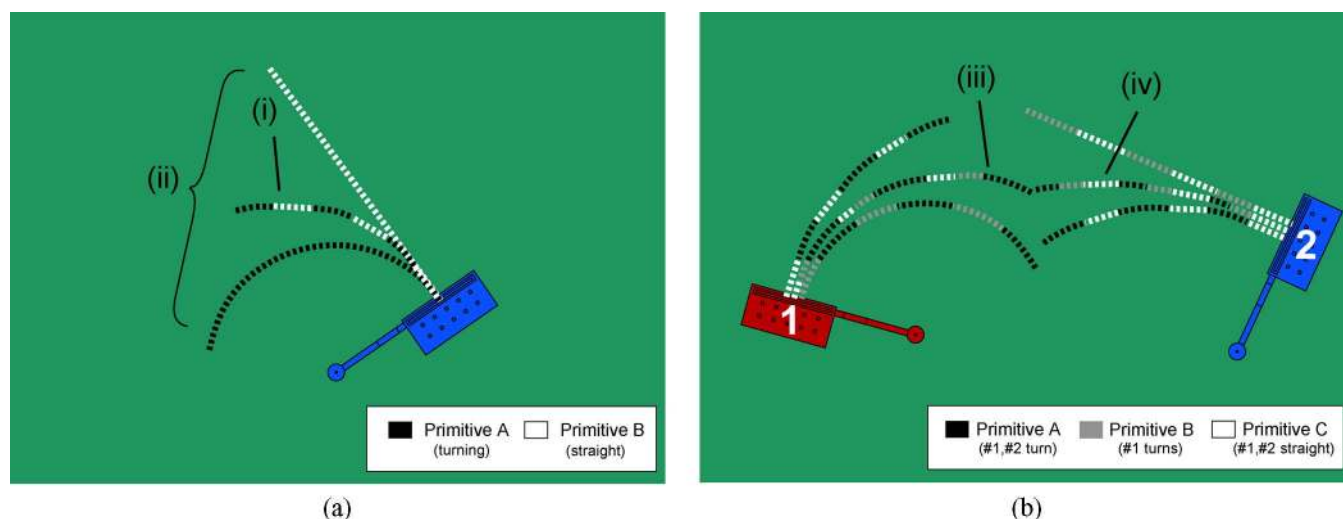


Fig. 12. Illustration of preimage trajectories. (a) Docking of a single microrobot with a stable shape. Corrections to the single robot trajectory are performed by adjusting the ratio between primitives A and B (turning and straight-line motion) in the control sequence defining the preimage trajectory (i). Error-correction cone (ii) indicates the maximum accumulated error that can be corrected for by adjusting the preimage trajectory. (b) Docking of two microrobots forming the initial stable shape. Preimage trajectories for the two robots (iii, iv) can be adjusted by varying the ratio between primitives A, B, and C. The trajectory of robot 1 (iii) can be adjusted without affecting the trajectory of robot 2 by adjusting the ratio between primitives B and C. Similarly, adjusting the ratio between primitives A and B allows the correction to the trajectory of robot 2 (iv) without affecting the trajectory of robot 1.

cone (ii) for a single microrobot. Wider cones allow for more adjustment to the preimage trajectory, hence permit error correction.

Error correction during the assembly of the initial stable shape is similar to single-device error correction. The trajectories of the two robots are divided into two parts, as previously described. Error correction in the first part of the trajectory execution is performed by periodically replanning the trajectories for both microrobots (using current configurations of the robots as new starting locations). Error correction during the second part of their trajectories is possible because preimage trajectories for parallel control of two robots interleave three primitives, for example, A, B, and C, in Fig. 12(b). The error-correction cones are now smaller and are spanned by A–C, A–B, and

A–B, B–C interleaved trajectories. By changing the ratio of these control primitives, we can modify the trajectory of one microrobot without affecting the trajectory of the other robot.

Fig. 13 shows the assembly process with error correction for a system of $n = 3$ microrobots. Panel (a) shows the docking of robots 2 and 3 forming the initial assembly, whereas robot 1 orbits in a circular path. Panel (b) shows subsequent docking of robot 1 to form the final shape.

By using two-part trajectories in our experiments, we have achieved an average docking misalignment of $3 \mu\text{m}$ (with $3 \mu\text{m}$ standard deviation) in docking of a single robot to a stable structure. In the case of two robots forming the initial stable shape, the average docking misalignment was $6 \mu\text{m}$ (with $7 \mu\text{m}$ standard deviation).

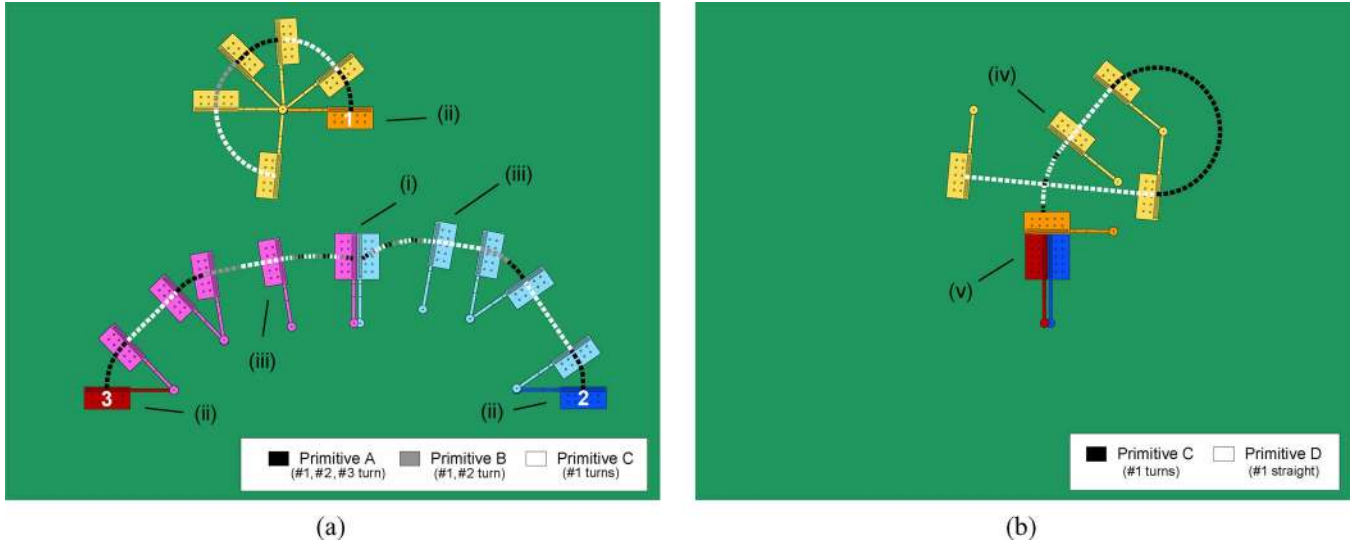


Fig. 13. Illustration of implementing microassembly using three microrobots. (a) Assembly of the initial stable shape (i) using microrobots (blue) 2 and (red) 3 while (orange) microrobot 1 orbits in a circular path. The trajectory of both robots starts in an initial configuration (ii) and passes through the preimage configuration (iii). The tracks are color-coded according to the primitive's ability to turn the microrobots that are being maneuvered. (b) Robot 1 is controlled [via the preimage configuration (iv)] to dock with the initial stable shape (i) forming the final assembly (v). Since only a single microrobot is controlled during the second stage, only two control primitives are used.

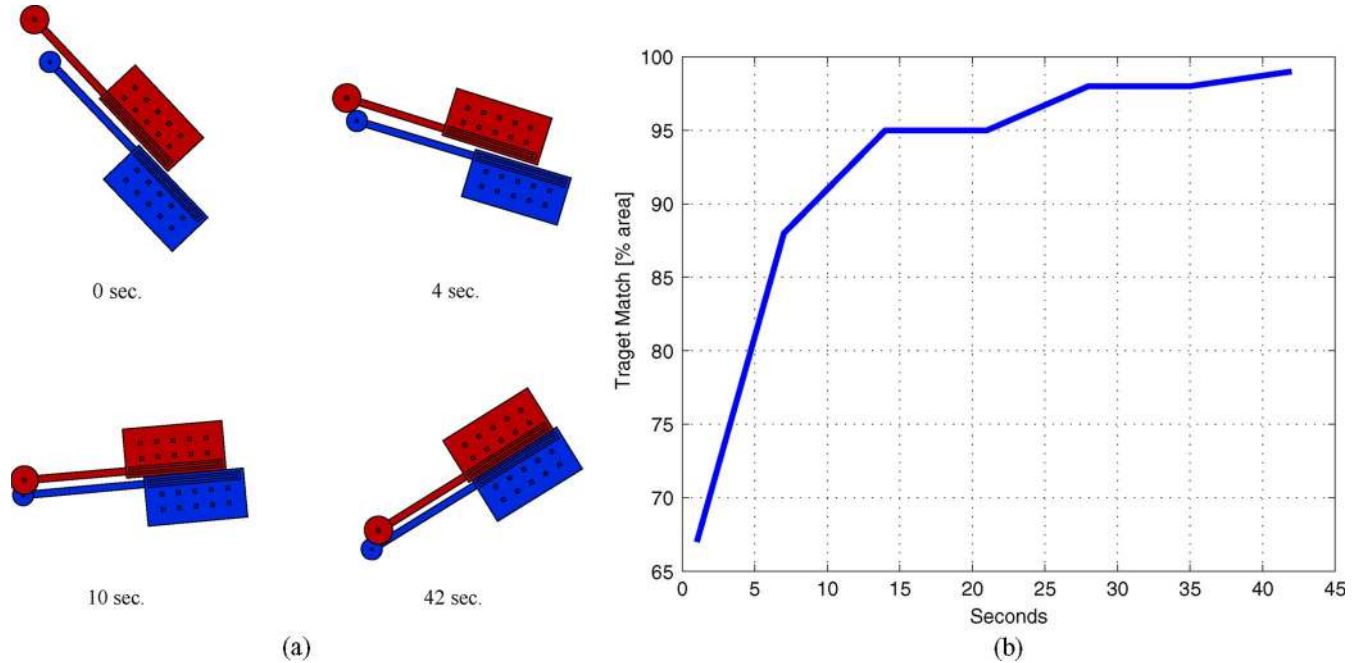


Fig. 14. Example of self-aligning compliance between two microrobots. (a) Outlines of a device from species (red) 4 and (blue) 5 recorded four times during a self-aligning experiment. (b) Plot of the percentage area of the target shape type G_1 (from Fig. 3) progressively covered by the assembled structure during the self-aligning experiment.

D. Self-Aligning Compliance

Misalignment of the initial stable shape is further reduced through self-aligning compliance. Two microrobots that dock to form the initial stable shape self-align during the application of a power-delivery waveform. The straight front edge of the SDA causes two opposing microrobots to slide relatively to one another until both robots reach a stable configuration. Self-alignment is a form of local pairwise SA. Fig. 14(a) shows an example of self-aligning between two docking robots. Outlines of the two devices measured four times during a self-aligning experiment are shown, illustrating the reduction in relative

misalignment. Note that the shape rotates as the two robots self-align. Fig. 14(b) shows the portion of the area of the target shape covered by the aligning structure during the experiment.

Combined error correction of the preimage trajectory and self-alignment result in a $2 \mu\text{m}$ average misalignment between two docking microrobots and enable the formation of nearly perfect initial stable shapes.

VI. MICROASSEMBLY EXPERIMENTS

We implemented microassembly using groups of four independent microrobots (described in Section V-A). Five








		Target Structure G					Average $G_1 - G_5$
		 G_1	 G_2	 G_3	 G_4	 G_5	
Initial Configuration	 R_1	96 % (4) 3 runs	98 % (3) 2 runs	96 % (2) 2 runs	96 % (na) 1 run	93 % (na) 1 run	96 % (3) 3 runs
	 R_2	99 % (2) 2 runs	98 % (na) 1 run	93 % (na) 1 run	89 % (na) 1 run	na	95 % (4) 2 runs
Average R_1 and R_2		97 % (3) 5 runs	98 % (2) 3 runs	95 % (2) 3 runs	93 % (5) 2 runs	93 % (na) 1 run	96 % (3) 5 runs

Fig. 15. Precision of microassembly. Table showing average match (portion of the area of the target shape covered by the assembled structure) for each of the generated shapes. See Fig. 3 for optical micrographs of the generated structures $G_1 - G_5$. A total of five assembly experiments were conducted starting from two classes of initial configurations R_1 and R_2 , namely, R_1 —robots are arranged in a square and R_2 —robots are arranged in a line. The standard deviation (in parenthesis) and the number of experimental runs from each class of initial configurations are also reported. Columns show identical shapes generated from different initial conditions, and rows show different shapes generated from the same initial conditions, illustrating the importance of control signal in our assembly process. The average match across all assembly experiments was 96%, with a standard deviation of 3%.

independent assembly experiments were conducted using groups (1, 3, 4, 5) and (2, 3, 4, 5), generating a total of 14 mesoscale structures. The robots were operated on a 2-mm² environment, and their position was observed using a digital video camera (Pixelink PL-A642). The position of the devices was extracted with a precision of $\pm 2.1 \mu\text{m}$. During the operation of the microrobots, the humidity was controlled below 4% relative humidity using a continuous stream of dry nitrogen. The waveforms defining the control primitives were produced by using an Agilent 33120A arbitrary waveform generator and amplified with a Trek PZD700-1 high-voltage power amplifier with a gain of 200.

Fig. 15 shows the average match (portion of the target structure covered by the assembled shape) for each type of generated shapes. The experiments were conducted starting from two different classes of initial configurations (region R in preimage⁴ notation), namely, R_1 —robots are arranged along the corners of a rectangle with sides 1 by 0.9 mm; all devices are oriented along the y -axis (see Fig. 16(a) for a representative example), and R_2 —robots are arranged in a line with average separation of 360 μm and variable orientation (see Fig. 17(a) for a representative example). The initial position of the microrobots was set using microprobes. We used common geometric shapes (a line and a rectangle) to demonstrate the ability to achieve successful assembly from arbitrary different initial configurations. Five types of planar structures were assembled, which are denoted as $G_1 - G_5$ (see Fig. 3). Because of our limited (2 mm²) operating environment, we relaxed the position and orientation of the initial stable shape during our experiments. Due to the absence of external fixtures that would constrain the position of the assembled structure, we consider the assembly a success regardless of the pose of the assembled structure, as long as the structure is entirely contained within the operating environment.

The average match across all assembled structures was 96%, with a standard deviation of 3%. This average does not include completely failed assemblies. We recorded an 11% failure rate during the consecutive assembly of nine structures over the course of three assembly experiments. The assembly of one of the nine structures failed due to the loss of stability of an intermediate structure, which was attributed to an initial unfortunate misalignment between the microrobots forming the intermediate assembly.

The average docking misalignment across all experiments was 5 μm with a standard deviation of 5 μm . In all experiments, compliance was used to self-align the initial stable structures. Two experiments were conducted with the initial shape purposefully misaligned by at least 50 μm to test the self-alignment. In these two experiments, the average misalignment after completed self-alignment was 9 μm (with 8 μm standard deviation). In the remaining three initial shape docking experiments, precise control was applied to minimize the initial misalignment. In these experiments, the average docking misalignment was 6 μm (with 7 μm standard deviation) before the self-alignment and 2 μm (with 3 μm standard deviation) after the self-alignment was complete.

When docking a single robot with a stable structure, the average docking misalignment was 3 μm (with 3 μm standard deviation), which is on the order of the minimum feature size of the fabrication process. The high precision at which we can achieve docking demonstrates the fidelity of the two-part docking trajectory.

Figs. 16 and 17 show two of the five assembly experiments, including the progressive assembly of stable structures. Each of the two experiments terminated when all four microrobots were successfully incorporated in the assembled structure, resulting in planar structures of types G_5 and G_3 , respectively. A movie of a representative assembly experiment is available online [48], [49].

⁴See Appendix. Definition of Terms.

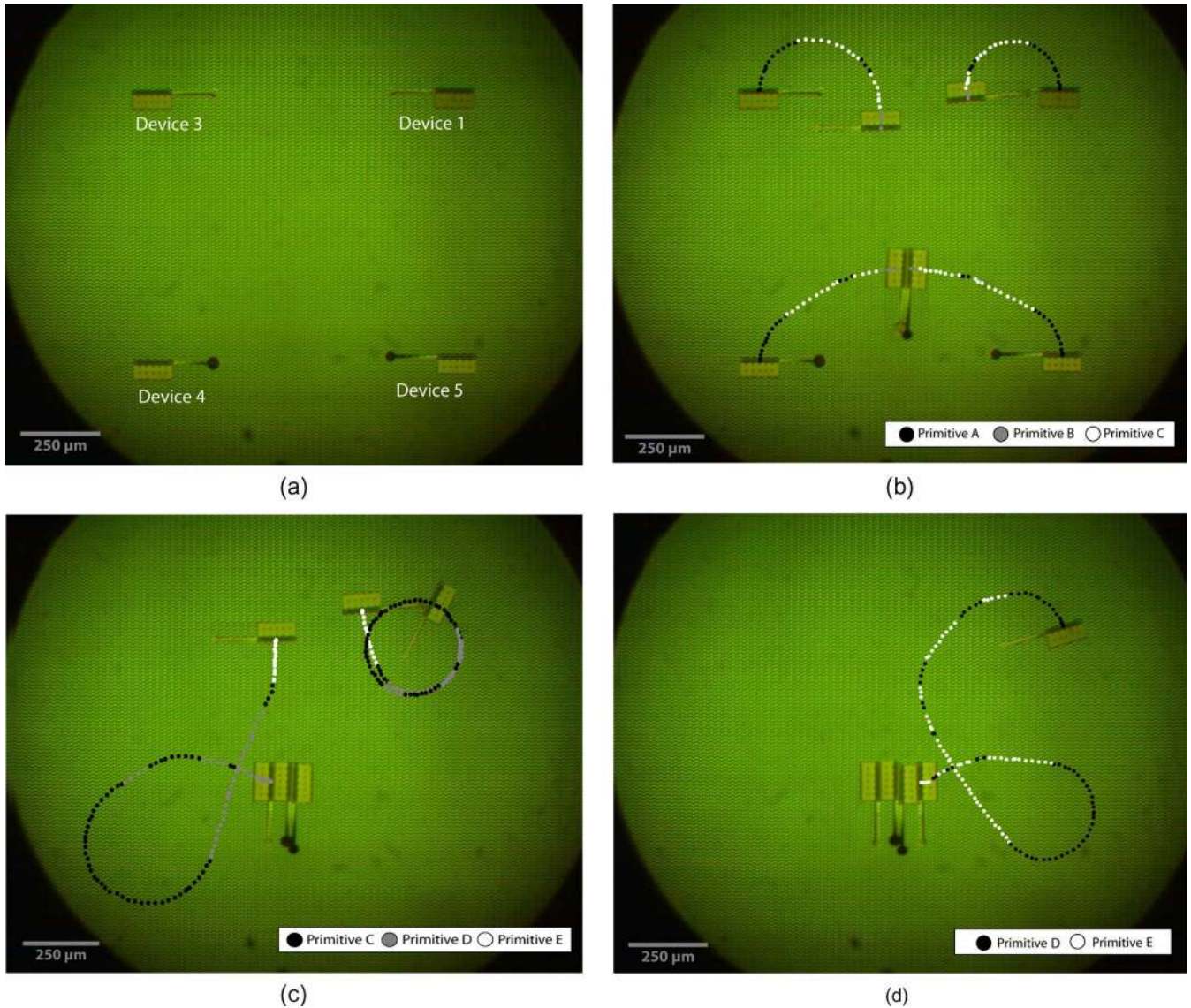


Fig. 16. Composite optical micrograph of experimental assembly data using devices from species 1, 3, 4, and 5. The devices are labeled according to the number of their respective species. (a) Initial configuration of the microrobots on the operating environment. (b) Docking of devices 4 and 5 to form the initial stable shape while devices 1 and 3 orbit. (c) Docking of device 3 with the initial stable shape while device 1 orbits. (d) Docking of device 1. Tracks showing the trajectories of the microrobots are annotated with respect to the number of robots that are being controlled during the particular stage of the assembly algorithm. Black denotes trajectory segments where both robots turn, gray denotes segments where one robot moves straight while the remaining robot turns, and white denotes segments where both robots move straight.

VII. LIMITATIONS AND EXTENSIONS

The work presented in this paper represents the first implementation of an interacting microscale multirobotic system and a new type of microassembly. As discussed in Section V, our planning and control scheme is not completely general since the periodic replanning based on EDR is not guaranteed. However, the control scheme was adequate to efficiently implement microassembly using our microrobots. Developing a general control scheme would be a useful future work.

The structural integrity of the generated assemblies is maintained through mutual compliance, static friction, and electrostatic attraction to the substrate. Methods such as reflow of solder, for example, used in templated SA [11], or mechanical snap-fasteners [6], [50] could be used to provide a

permanent connection between the docked devices. The implementations of such docking mechanisms for our microrobots would be a valuable future extension. It should be noted that even intermittently rigid structures could be used as physical authentication functions for implementing nonelectronic-based security systems, such as, for example, optical cryptography [51], [52] or other systems that rely on the formation of patterns rather than rigid structures.

Although both the fabrication process and the operating environment can potentially be improved, the number of independent transition voltages does not scale. However, the control strategy presented in Section V can be applied to systems of up to n microrobots, where $n \leq kl$. This is a significant advance over our previously proposed approach [1], where $n \leq k = l$. An interesting future work would be to

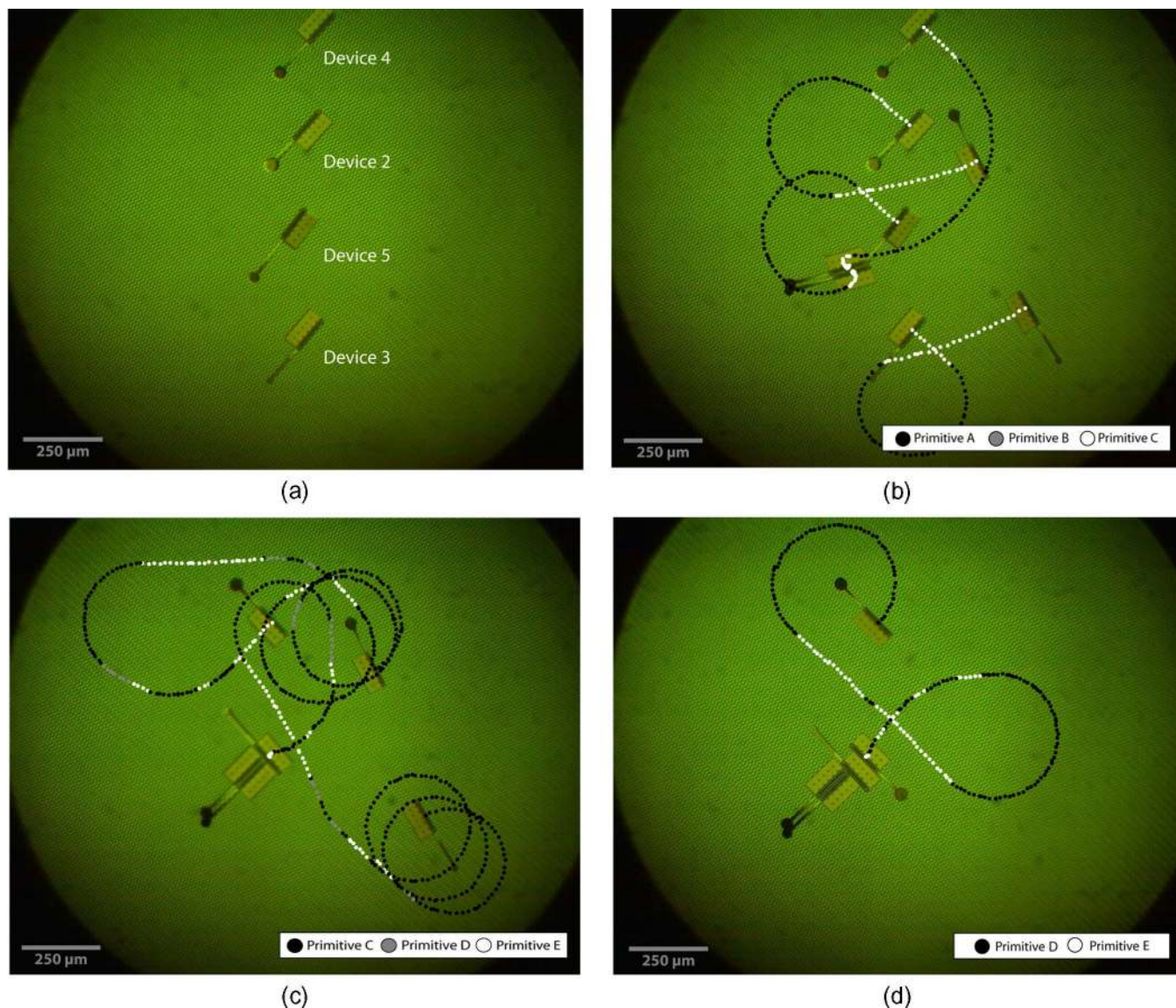


Fig. 17. Composite optical micrograph of experimental assembly data using devices from species 2, 3, 4, and 5. The devices are labeled according to the number of their respective species. **(a)** Initial configuration of the microrobots, which are positioned along a line within the operating environment. **(b)** Trajectory of devices 4 and 5 forming the initial stable shape while devices 2 and 3 orbit. Devices 4 and 5 move along a trajectory to a common intersection point. The large ($80\ \mu\text{m}$) initial misalignment causes the initial stable structure to rotate by over 90° . Primitive E is applied for 10 s to separate the devices before starting the assembly trajectories. After devices 4 and 5 make contact, primitive E is applied for 25 s to promote self-aligning of the initial shape; during this time, devices 2 and 3 move straight and away from the self-aligning shape. **(c)** Docking of robot from species 3 with the initial stable shape. After following a circular trajectory, device 2 is moved to the left to avoid the preimage trajectory of device 3. Both devices 2 and 3 complete several full circles until they are aligned in favorable directions and can be moved in parallel (primitive E.) **(d)** Docking of robot 2 with the stable structure, completing the assembly experiment. Black denotes trajectory segments where both robots currently controlled via the assembly algorithm turn, gray denotes segments where one robot moves straight while the remaining robot turns, and white denotes segments where both robots move straight. Primitive B was used to control turning of both devices 2 and 3 because it produced a tighter radius of curvature and more reliable turning behavior in device 2 than primitive C or D.

investigate other mechanisms that allow us to differentiate the behavior of individual microrobots through a common control signal.

MEMS fabrication is an inherently parallel fabrication process; however, our single-device trimming is an inherently serial procedure. Trimming is not intended to scale because its purpose is to be used infrequently to adjust a few individual devices within a large batch of robots. If more than few devices need adjustment, it may be more efficient to discard the entire batch. It is conceivable that a shadow-mask structure matching each transfer frame could be fabricated; the transition voltages can be tested without releasing the devices from the transfer

frames, and a batch trimming process could be performed. In the future, chrome deposition through parallel shadow-masking could be used to eliminate the pre-release stress-engineering process with its inherent GA issues.

Finally, the compliance model of docking microrobots is empirically parameterized based on observed data. The scalability of this model needs to be confirmed in order to allow us to predict the assembly sequence for shapes made out of more than four devices. In particular, a mechanics model (e.g., [53]) that determines the forces acting between the docked devices within the structure would be useful to predict the stability of intermediate and final assemblies.

VIII. CONCLUSION

In this paper, we have demonstrated the first example of parallel operation of multiple untethered MEMS microrobots. We presented designs and fabrication of independent stress-engineered microrobot species, as well as control algorithms that implement a new microassembly scheme, generating planar structures with a high level of accuracy. The average match between the generated structures versus the desired target configurations was 96%, with an average misalignment of 5 μm across all experiments and 3 μm in experiments where error correction and self-aligning compliance were fully implemented. Note that 3 μm is on the order of the minimum feature size of the microrobot fabrication process.

The high accuracy of assembly combined with the variety of structures assembled on a small (1.4 \times 1.4 mm) operating environment demonstrates the feasibility of the proposed microassembly scheme to generate structures composed of simple microfabricated components. Parallel control of a highly underactuated microrobotic system is an essential part of our microassembly paradigm. In the presence of a global broadcast-type control signal, a multi-microrobotic system composed of many single units will naturally be highly underactuated, necessitating the type of control algorithms presented in this paper. Successful control of highly underactuated systems is likely to be important as the size of the assembling components is reduced even further, noting that parallel operation, broadcast communication, and selective response are commonplace in the architecture of micro- and nanoscale biological systems. Consequently, our control scheme may perhaps also be applied to the assembly of other micro- and nanoscale structures.

APPENDIX DEFINITION OF TERMS

Configuration space (C-space): The C-space of a rigid body [54] is the set of all possible poses of that body within its workspace. For a planar, rigid, and laminar body, this is equivalent to position (\mathbb{R}^2) and orientation (S^1), in the C-space $\mathbb{R}^2 \times S^1$. The C-space of n planar rigid bodies is the set of all possible poses of the bodies, which is formally $(\mathbb{R}^2 \times S^1)^n$.

Global controllability: The ability of a system to access all of its C-space. In the case of a single mobile microrobot [1], it is the ability to reach any position and orientation (in the absence of obstacles) [55].

Nonholonomic system: (in the context of this paper) A mobile robotic system with nonholonomic motion constraints, which are constraint equations involving the time derivatives of the configuration variables [45]. A car, bicycle, or our microrobots are all examples of nonholonomic systems, as these devices can only move in the direction that they are facing.

Small-time local controllability (STLC): A system is small-time locally controllable (STLC) if for any configuration q and for any neighborhood U of q , there exists a neighborhood V of q , such that there is a path from q to every configuration in V that lies entirely within U [45]. Our microrobot is not STLC because it can only turn one way and cannot move backward.

Strong preimage: The strong preimage $P_{\theta,R}(G)$ is the region in C-space C from which a control strategy θ is guaranteed to terminate in the goal region G given the initial conditions $R \subset C$ [46].

Underactuated system: A system where the number of control parameters is less than the number of the DOF.

ACKNOWLEDGMENT

The electron micrographs were taken at the Dartmouth Ripple Electron Microscopy Laboratory, with the help of C. P. Daghljan. The authors would like to thank D. Rus for her advice and collaboration, C. McGray for the initial work on the stress-engineered MEMS microrobot, and U. J. Gibson for the use of equipment in her laboratory and for many helpful discussions. The authors would also like to thank D. Balkcom, C. Bailey-Kellogg, A. Lebeck, K. Böhringer, and J. Reif for their advice and suggestions.

REFERENCES

- [1] B. R. Donald, C. G. Levey, C. McGray, I. Paprotny, and D. Rus, "An untethered, electrostatic, globally controllable MEMS micro-robot," *J. Microelectromech. Syst.*, vol. 15, no. 1, pp. 1–15, Feb. 2006.
- [2] B. R. Donald, C. G. Levey, C. McGray, D. Rus, and M. Sinclair, "Power delivery and locomotion of untethered microactuators," *J. Microelectromech. Syst.*, vol. 12, no. 6, pp. 947–959, Dec. 2003.
- [3] M. T. Mason, *Mechanics of Robotic Manipulation*. Cambridge, MA: MIT Press, 2001.
- [4] D. Koester, A. Cowen, R. Mahadevan, M. Stonefield, and B. Hardy, *PolyMUMPs Design Handbook, A MUMPs Process*, 10th ed. Grenoble, France: MEMSCAP, 2003.
- [5] H. C. Nathanson, W. E. Newell, R. A. Wickstrom, and J. J. R. Davis, "The resonant gate transistor," *IEEE Trans. Electron Devices*, vol. ED-14, no. 3, pp. 117–133, Mar. 1967.
- [6] N. Dechev, W. L. Cleghorn, and J. K. Mills, "Tether and joint design for micro-components used in microassembly of 3D microstructures," in *Proc. SPIE—Micromachining and Microfabrication, Photonics West*, Jan. 2004, pp. 134–146.
- [7] G. Skidmore, M. Ellis, A. Geisberger, K. Tsui, K. Tuck, R. Saini, T. Udeshi, M. Nolan, R. Stallcup, and J. Von Ehr, II, "Assembly technology across multiple length scales from the micro-scale to the nano-scale," in *Proc. 17th IEEE Int. Conf. MEMS*, 2004, pp. 588–592.
- [8] G. M. Whitesides and B. Grzybowski, "Self-assembly at all scales," *Science*, vol. 295, no. 5564, pp. 2418–2421, Mar. 2002.
- [9] E. Winfree, F. Liu, L. A. Wenzler, and N. C. Seeman, "Design and self-assembly of two-dimensional DNA crystals," *Nature*, vol. 394, no. 6693, pp. 539–544, Aug. 1998.
- [10] P. W. K. Rothmund, "Using lateral capillary forces to compute by self-assembly," *Proc. Nat. Acad. Sci. U.S.A.*, vol. 97, no. 3, pp. 984–989, Feb. 2000.
- [11] S. H. Liang, X. Xioang, and K.-F. Böhringer, "Towards optimal designs for self-alignment in surface tension driven micro-assembly," in *Proc. IEEE Conf. MEMS*, Jan. 2004, pp. 9–12.
- [12] D. Popa and H. E. Stephanou, "Micro and meso scale robotic assembly," *SME J. Manuf. Processes*, vol. 6, no. 1, pp. 52–71, 2004.
- [13] K. E. Drexler, "Molecular manufacturing: Perspectives on the ultimate limits of fabrication," *Philos. Trans. R. Soc. Lond. A, Math. Phys. Sci.*, vol. 353, no. 1703, pp. 323–331, Dec. 1995.
- [14] K.-F. Böhringer, B. R. Donald, R. R. Mihailovich, and N. C. MacDonald, "A theory of manipulation and control for microfabricated actuator arrays," in *Proc. IEEE Workshop MEMS*, Jan. 1994, pp. 102–107.
- [15] K. F. Böhringer, B. R. Donald, and N. C. MacDonald, "Programmable force fields for distributed manipulation, with applications to MEMS actuator arrays and vibratory parts feeders," *Int. J. Rob. Res.*, vol. 18, no. 2, pp. 168–200, 1999.
- [16] J. W. Suh, R. B. Daring, K. F. Böhringer, B. R. Donald, H. Baltes, and G. T. A. Kovacs, "CMOS integrated ciliary actuator array as a general-purpose micromanipulation tool for small objects," *J. Microelectromech. Syst.*, vol. 8, no. 4, pp. 483–496, Dec. 1999.

- [17] E. Winfree, "Algorithmic self-assembly of DNA: Theoretical motivations and 2D assembly experiments," *J. Biomol. Struct. Dyn.*, vol. 11, no. 2, pp. 263–270, Jun. 2000.
- [18] H. Onoe, K. Matsumoto, and I. Shimoyama, "Three-dimensional micro-self-assembly using hydrophobic interaction controlled by self-assembled monolayers," *J. Microelectromech. Syst.*, vol. 13, no. 4, pp. 603–611, Aug. 2004.
- [19] M. Hori and S. Hashimoto, "Self-Assembly of micro parts by controlling the environmental parameters," in *Proc. Int. Symp. Micromechatronics Human Sci.*, 2003, pp. 189–195.
- [20] S. Bagilo, S. Castorina, L. Fortuna, and N. Savalli, "Technologies and architectures for autonomous MEMS microrobot," in *Proc. IEEE ISCAS*, May 2002, vol. 2, pp. II-584–II-587.
- [21] P. E. Kladitis and V. M. Bright, "Prototype microrobots for micro-positioning and micro-unmanned vehicles," *Sens. Actuators A, Phys.*, vol. 80, no. 2, pp. 132–137, Mar. 2000.
- [22] S. Hollar, A. Flynn, C. Bellew, and K. S. J. Pister, "Solar powered 10 mg silicon robot," in *Proc. 16th Annu. Int. Conf. MEMS*, Kyoto, Japan, Jan. 19–23, 2003, pp. 706–711.
- [23] P. Dario, R. Valleggi, M. C. Carrozza, M. C. Montesi, and M. Cocco, "Microactuators for microrobots: A critical survey," *J. Micromech. Microeng.*, vol. 2, no. 3, pp. 141–157, Sep. 1992.
- [24] J. M. Kahn, R. H. Katz, and K. S. J. Pister, "Mobile networking for smart dust," in *Proc. ACM/IEEE Int. Conf. MobiCom Netw.*, Seattle, WA, Aug. 17–19, 1999, pp. 17–19.
- [25] K. B. Yesin, K. Vollmers, and B. J. Nelson, "Modeling and control of untethered bio-inspired microrobots in fluid environment using electromagnetic fields," *Int. J. Rob. Res.*, vol. 25, no. 5/6, pp. 527–536, May/June 2006.
- [26] K. Kotay and D. Rus, "Locomotion versatility through self-reconfiguration," *Robot. Auton. Syst.*, vol. 26, no. 2, pp. 217–232, Feb. 1999.
- [27] D. Rus, "Self-reconfiguring robots," *IEEE Intell. Syst.*, vol. 13, no. 4, pp. 2–4, Jul./Aug. 1998.
- [28] Z. Butler, R. Fitch, and D. Rus, "Distributed control for unit-compressible robots: Goal-recognition, locomotion, and splitting," *IEEE/ASME Trans. Mechatronics*, vol. 7, no. 4, pp. 418–430, Dec. 2002.
- [29] D. Rus, B. R. Donald, and J. Jennings, "Moving furniture with teams of autonomous mobile robots," in *Proc. IEEE/Robot. Soc. Jpn. Int. Workshop IROS*, Pittsburg, PA, 1995, pp. 235–242.
- [30] B. R. Donald, J. Jennings, and D. Rus, "Information invariants for distributed manipulation," *Int. J. Rob. Res.*, vol. 16, no. 5, pp. 673–702, Oct. 1997.
- [31] D. Stilwell and J. Bay, "Toward the development of a material transport system using swarms of ant-like robots," in *Proc. IEEE Int. Conf. Robot. Autom.*, Atlanta, GA, 1993, pp. 766–771.
- [32] E. Pagello, A. D'Angelo, F. Montesello, F. Garelli, and C. Ferrari, "Cooperative behaviors in multi-robot systems through implicit communication," *Robot. Auton. Syst.*, vol. 29, no. 1, pp. 65–77, Oct. 1999.
- [33] A. Jadbabaie, J. Lin, and A. S. Morse, "Coordination of groups of mobile autonomous agents using nearest neighbor rules," *IEEE Trans. Autom. Control*, vol. 48, no. 6, pp. 988–1001, Jun. 2003.
- [34] A. Martinoli and K. E. W. Agassounon, "Modeling swarm robotic systems: A case study in collaborative distributed manipulation," *Int. J. Rob. Res.*, vol. 23, no. 4/5, pp. 415–436, Apr. 2004.
- [35] B. R. Donald, *Building Very Small Mobile Micro-Robots*, ser. Inaugural Lecture, Nanotechnology Public Lecture Series. Cambridge, MA: Res. Lab. Electron., EECS, Microsystems Technol., Lab., MIT, Apr. 2007. [Online]. Available: <http://mitworld.mit.edu/video/463/>
- [36] E. Schierenberg, *Embryological variation during nematode development*, T. E. Community, Ed. Wormbook, 2006. [Online]. Available: <http://www.wormbook.org>
- [37] T. Bretl, "Control of many agents using few instructions," in *Proc. Robot. Sci. Syst. Conf.*, Atlanta, GA, 2007.
- [38] L. E. Dubins, "On curves of minimal length with a constraint on average curvature, and with prescribed initial and terminal positions and tangents," *Am. J. Math.*, vol. 79, no. 3, pp. 497–516, Jul. 1957.
- [39] T. Akiyama and K. Shono, "Controlled stepwise motion in polysilicon microstructures," *J. Microelectromech. Syst.*, vol. 2, no. 3, pp. 106–110, Sep. 1993.
- [40] O. N. Pierron, D. D. Macdonald, and C. L. Muhlstein, "Galvanic effects in Si-based microelectromechanical systems: Thick oxide formation and its implications for fatigue reliability," *Appl. Phys. Lett.*, vol. 86, no. 21, p. 21119, May 1995.
- [41] E. K. L. Chan, "Characterization and modeling of electrostatically actuated polysilicon micromechanical devices," Ph.D. dissertation, Elect. Eng. Dept., Stanford Univ., Stanford, CA, 1999.
- [42] H. Kahn, C. Deeb, I. Chasiotis, and A. H. Heuer, "Anodic oxidation during MEMS processing of silicon and polysilicon: Native oxides can be thicker than you think," *J. Microelectromech. Syst.*, vol. 14, no. 5, pp. 914–923, Oct. 2005.
- [43] L. Torcheux, A. Mayeux, and M. Chemla, "Electrochemical coupling effects on the corrosion of silicon samples in HF solutions," *J. Electrochem. Soc.*, vol. 142, no. 6, pp. 2037–2046, Jun. 1995.
- [44] G. Stoney, "The tension of metallic films deposited by electrolysis," *Proc. R. Soc. Lond. A*, vol. 82, no. 553, pp. 172–175, May 1909.
- [45] J.-P. Laumond, *Robot Motion Planning and Control*. New York: Springer-Verlag, 1998.
- [46] T. Lozano-Perez, M. T. Mason, and R. H. Taylor, "Automatic synthesis of fine-motion strategies for robots," AI Lab., MIT, Cambridge, MA, A. I. Memo 759, Dec. 1983.
- [47] B. R. Donald, *Error Detection and Recovery in Robotics*, vol. 336. New York: Springer-Verlag, 1987.
- [48] B. R. Donald, C. G. Levey, and I. Paprotny, *Planar Microassembly by Parallel Actuation of MEMS Microrobots—Supplementary Video*. Durham, NC: Dept. Comput. Sci., Duke Univ., 2008. [Online]. Available: www.cs.duke.edu/donaldlab/Supplementary/jmms08/
- [49] B. R. Donald, C. G. Levey, and I. Paprotny, "Planar Microassembly by Parallel Actuation of MEMS Microrobots—Supplementary Video," Dept. Comput. Sci., Dartmouth College, Hanover, NH, 2008. Tech. Rep. [Online]. Available: www.cs.dartmouth.edu/reports/abstracts/2008.shtml
- [50] R. Prasad, K.-F. Böhringer, and N. C. MacDonald, "Design, fabrication, and characterization of single crystal silicon latching snap fasteners for micro assembly," in *Proc. ASME IMECE*, Nov. 1995, pp. 917–923.
- [51] J.-Y. Kim, S.-J. Park, C.-S. Kim, J.-G. Bae, and S.-J. Kim, "Optical image encryption using interferometry-based phase masks," *Electron. Lett.*, vol. 36, no. 10, pp. 874–875, May 2000.
- [52] W.-O. Kwok, N.-K. Bao, A. H.-P. Chan, and P. Wong, "Cryptography of e-beam generated digital pixel holography," in *Proc. 6th Int. Conf. Solid-State Integr.-Circuit Technol.*, Oct. 2001, pp. 471–486.
- [53] M. Erdmann, "On a representation of friction in configuration space," *Int. J. Robot. Res.*, vol. 13, no. 6, pp. 240–271, 1994.
- [54] T. Lozano-Perez and M. A. Wesley, "An algorithm for planning collision-free paths among polyhedral obstacles," *Commun. ACM*, vol. 22, no. 10, pp. 560–570, Oct. 1979.
- [55] H. Hermes, "On local and global controllability," *SIAM J. Control*, vol. 12, no. 2, pp. 252–261, 1974.
- [56] T. Akiyama, D. Collard, and H. Fujita, "Scratch drive actuator with mechanical links for self-assembly of three-dimensional MEMS," *J. Microelectromech. Syst.*, vol. 6, no. 1, pp. 10–17, Mar. 1997.
- [57] L. Li, J. G. Brown, and D. Uttamchandani, "Detailed study of scratch drive actuator characteristics using high-speed imaging," in *Proc. SPIE—Reliability, Testing, Characterization of MEMS/MOEMS*, 2001, vol. 4558, pp. 117–123.
- [58] R. J. Linderman and V. M. Bright, "Nanometer precision positioning robots utilizing optimized scratch drive actuators," *Sens. Actuators A, Phys.*, vol. 91, no. 3, pp. 292–300, Jul. 2001.



Bruce R. Donald (S'85–M'87) received the B.A. degree (*summa cum laude*) from Yale University, New Haven, CT, and the S.M. and Ph.D. degrees from Massachusetts Institute of Technology (MIT), Cambridge, MA.

Previously, he held faculty positions at Dartmouth and Cornell. He has been a National Science Foundation Presidential Young Investigator. He has worked in several research areas, including robotics, microelectromechanical systems, computational biology, graphics, and geometric algorithms. He is the William and Sue Gross Professor of Computer Science with the Department of Computer Science, Duke University, Durham, NC, and he is also a Professor of Biochemistry with the Department of Biochemistry, Duke University Medical Center, Durham. He was awarded a Guggenheim Fellowship for his work on algorithms for structural proteomics. He has held visiting and research positions at Harvard, Stanford, Interval Research Corporation, and MIT.



Christopher G. Levey (A'93–M'03) received the B.A. degree from Carleton College, Northfield, MN, in 1977, and the Ph.D. degree in physics from the University of Wisconsin, Madison, in 1984.

He was a Member of Technical Staff with AT&T Bell Laboratories until 1986, when he became a Professor with the Physics Department, Dartmouth College, Hanover, NH, where he continues to hold a joint appointment. He is an Associate Professor of engineering and the Director of the Microengineering Laboratory, Thayer School of Engineering, Dartmouth College. His research has included laser spectroscopy, superconductor devices, stress-engineered microelectromechanical system (MEMS) structures, binary optics, programmable microvapor dispensers, integrated inductors, and MEMS-based robots.



Igor Paprotny received the Engineering Diploma in mechatronics from the NKI College of Engineering, Oslo, Norway, and the B.S. and M.S. degrees in industrial engineering from Arizona State University, Tempe. He is currently working toward the Ph.D. degree in the Department of Computer Science, Dartmouth College, Hanover, NH, and is in residence with the Department of Computer Science, Duke University, Durham, NC, both working under the direction of Prof. Bruce Donald.

He has over three years of professional experience in the semiconductor industry, where he was involved in optimization and automation of several manufacturing operations. His research involves microrobotics, physical computation paradigms, and microelectromechanical system.